

# Petit-spot lavas on the western Pacific Plate: contribution of carbonatite and recycled oceanic crust

Kazuto Mikuni<sup>1,2,\*</sup>, Naoto Hirano<sup>2,3</sup>, Shiki Machida<sup>4</sup>, Hirochika Sumino<sup>5</sup>, Norikatsu Akizawa<sup>6</sup>, Akihiro Tamura<sup>7</sup>, Tomoaki Morishita<sup>7</sup>, Yasuhiro Kato<sup>4,8,9</sup>

<sup>1</sup> AIST, Geological Survey of Japan, Research Institute of Geology and Geoinformation, Central 7, 1-1-1, Higashi, Tsukuba, Ibaraki 305-8567, Japan.

<sup>2</sup> Graduate School of Science, Tohoku University, 6-3 Aramaki-Aoba, Aoba-ku, Sendai 980-8578, Japan.

<sup>3</sup> Center for Northeast Asian Studies, Tohoku University, 41 Kawauchi, Aoba-ku, Sendai 980-8576, Japan.

<sup>4</sup> Ocean Resources Research Center for Next Generation, Chiba Institution of Technology, 2-17-1 Tsudanuma, Narashino 275-0016, Japan.

<sup>5</sup> Research Center for Advanced Science and Technology, the University of Tokyo, 4-6-1 Komaba, Meguro-ku, Tokyo 153-8904, Japan

<sup>6</sup> Atmosphere and Ocean Research Institute, the University of Tokyo, 5-1-5, Kashiwanoha, Kashiwa 277-8564, Japan.

<sup>7</sup> Earth Science Course, Kanazawa University, Kakuma, Kanazawa 920-1192, Japan.

<sup>8</sup> Department of Systems Innovation, School of Engineering, The University of Tokyo, 7-3-1 Hongo, Bunkyo-ku, Tokyo 113-8656, Japan.

<sup>9</sup> Submarine Resources Research Center, Research Institute for Marine Resources Utilization, Japan Agency for Marine-Earth Science and Technology (JAMSTEC), 2-15 Natsushima-cho, Yokosuka, Kanagawa, 237-0061, Japan.

\* Correspondence to Kazuto Mikuni (kazuto.mikuni @aist.go.jp)

Authors' e-mail addresses and ORCiD numbers

Kazuto Mikuni<sup>1,\*</sup> kazuto.mikuni@aist.go.jp 0000-0001-6939-4333

Naoto Hirano<sup>2,3</sup> nhirano@tohoku.ac.jp 0000-0003-0980-3929  
Shili Meng<sup>1,4</sup> shili-meng@lilac.tohoku.ac.jp 0000-0002-1862-7214

Shiki Machida<sup>4</sup> shiki.machida@p.chibakoudai.jp 0000-0002-1069-7214  
Hirochika Sumino<sup>5</sup> sumino@icgl.e.u.tokyo.ac.jp 0000-0002-1689-6231

Toshihiko Sumino sumino@lgci.ecc.u-tokyo.ac.jp 0000-0002-4689-0231  
Norikatsu Akizawa<sup>6</sup> akizawa@g.ecc.u-tokyo.ac.jp 0000-0003-4210-1160

Noritatsu Akihiro Tamura [aking826@gmail.com](mailto:aking826@gmail.com) 0000-0002-9112-7976  
Akihiro Tamura<sup>7</sup> [aking826@gmail.com](mailto:aking826@gmail.com) 0000-0002-9112-7976

Tomoaki Morishita<sup>7</sup> moripta@gmail.com 0000-0002-8724-6868

Yasuhiro Kato<sup>4,8,9</sup>      [ykato@sys.t.u-tokyo.ac.jp](mailto:ykato@sys.t.u-tokyo.ac.jp)      0000-0002-5711-8304

---

The manuscript is going to be submitted to *Solid Earth*.

The manuscript is going to be submitted to *Solid Earth*.

40

41 **Keywords: Petit-spot volcano, alkali basalt, carbonatite, asthenosphere**

42

43 **Abstract**

44

45 Petit-spot volcanoes, which occurs owing occurring due to the plate flexure, have been  
46 reported from around the world globally. As the petit-spot melts ascend from the asthenosphere, they  
47 provide crucial the essential information of the lithosphere–asthenosphere boundary (LAB). Herein,  
48 we examined observed the lava outcrops of six monogenetic volcanoes formed by petit-spot volcanism  
49 in the western Pacific. Thereafter, we then determined analyzed the  $^{40}\text{Ar}/^{39}\text{Ar}$  ages, major and trace  
50 element compositions, and Sr, Nd, and Pb isotopic ratios of the petit-spot basalts. The  $^{40}\text{Ar}/^{39}\text{Ar}$  ages  
51 of two monogenetic volcanoes were ca. 2.6 Ma (million years ago) and ca. 0 Ma, respectively. The  
52 isotopic compositions of the western Pacific petit-spot basalts suggest geochemically similar melting  
53 sources. They were likely derived from a mixture of high- $\mu$  (HIMU) mantle-like and enriched mantle  
54 (EM)-1-like components related to carbonatitic/carbonated materials and recycled crustal components.  
55 A mass balance based melting model implied that The characteristic trace element composition (i.e.,  
56 Zr, Hf, and Ti depletions) of the western Pacific petit-spot magmas could be explained by the partial  
57 melting of ~5% crust-bearing garnet lherzolite with 10% carbonatite flux to a given mass of the source,  
58 as implied by a mass balance-based melting model. This result confirms the involvement of carbonatite  
59 melt and recycled crust in the source of petit-spot melts. It and provides an implication for insights into  
60 the genesis of tectonic-induced volcanoes, including Hawaiian North Arch volcanoes and Samoan  
61 petit-spot-like rejuvenated volcanoes, that have having similar trace element composition to petit-spot  
62 basalts.

63

64

65 **Short Summary**

66

67 Plate tectonics theory is understood as the motion of rocky plates (lithosphere) over ductile zones  
68 (asthenosphere). The causes of the lithosphere–asthenosphere boundary (LAB) is are  
69 controversial; however, but petit-spot volcanism supports the presence of melt at the LAB. We  
70 conducted geochemistry, geochronology, and geochemical modeling for of petit-spot volcanoes on the  
71 western Pacific Plate, and the results suggested that carbonatite melt and recycled oceanic crust have  
72 induced the partial melting at the LAB.

73

74 **1 Introduction**

75

76 Among the upper mantle-derived alkali basaltic lavas in oceanic settings, those on thicker plates  
77 away from the mid-ocean ridge, could be divided into plume-related and non-plume-related volcanoes.  
78 For example, plume-related North Arch and post-erosional (rejuvenated-stage) volcanoes have been  
79 reported in Hawaii and Samoa (Bianco et al., 2005; Bizimis et al., 2013; Clague and Frey, 1982; Clague  
80 and Moore, 2002; Dixon et al., 2008; Frey et al., 2000; Garcia et al., 2016; Hart et al., 2004; Konter  
81 and Jackson, 2012; Koppers et al., 2008; Reinhard et al., 2019; Yang et al., 2003). Non-plume-related  
82 intraoceanic alkali volcanoes, called known as petit-spot volcanoes, probably originate where nearby  
83 plate subduction causes plate flexures and upwelling of asthenospheric magma (Hirano et al., 2006;  
84 Hirano and Machida, 2022; Machida et al., 2015, 2017; Yamamoto et al., 2014, 2018, 2020). Therefore,  
85 The occurrence of petit-spot volcanisms supports the presence of melt at the lithosphere-  
86 asthenosphere boundary (LAB) below the area at least.

87 The presence of melt in the uppermost asthenosphere could be due to small-scale convection, heating, or the presence of hydrous or carbonatitic components, or the uplift  
88 of the lithosphere in response to plate flexure; however, the possibility of such an occurrence remains  
89 ambiguous (e.g., Bianco et al., 2005; Hua et al., 2023; Korenaga, 2020). In particular, The presence  
90 of CO<sub>2</sub> and carbonated/carbonatitic materials is a significant key factor in the formation of alkaline,  
91 silica-undersaturated melt in the upper mantle (Dasgupta and Hirschmann, 2006; Dasgupta et al., 2007,  
92 2013; Kisieva et al., 2013; Novella et al., 2014). Experimental studies have shown that the solidus of  
93 carbonate-bearing peridotite is lower than that of CO<sub>2</sub>-free peridotite (Falloon and Green, 1989, 1990;  
94 Foley et al., 2009; Ghosh et al., 2009). In addition, Moreover, carbonatites and Si-undersaturated melts  
95 are generated through the partial melting of CO<sub>2</sub>-bearing or carbonated peridotite. The produced melts  
96 could exhibit continuous chemical variations depending on pressure (i.e., depth). Namely,  
97 carbonatitic melts are produced in the deep asthenosphere (300 km to ~110 km), while carbonated  
98 or alkali silicate melts are generated in the shallower upper mantle (from ~110 km to ~75 or 60 km)  
99 (Keshav and Gudfinnsson, 2013; Massuyneau et al., 2015, 2021). Indeed, Primary carbonated silicate  
100 magma and evolved alkali basalts have been simultaneously observed at the post-spreading ridge in  
101 the South China Sea (Zhang et al., 2017; Zhong et al., 2021). The occurrence of Hawaiian rejuvenated  
102 volcanoes can be attributed to were also attributed to be explained by a carbonatite-metasomatized  
103 source with or without silicate metasomatism (Borisova and Tilhac, 2021; Dixon et al., 2008; Zhang  
104 et al., 2022).

106 Submarine petit-spot volcanoes on the subducting northwestern (NW) Pacific Plate may have  
107 originated from carbonate-bearing materials and crustal components (pyroxenite/eclogite) based on  
108 the characteristic trace elements, enriched mantle (EM)-1-like Sr, Nd, and Pb isotopic, and relatively  
109 low Mg isotopic compositions (Liu et al., 2020; Machida et al., 2009, 2015). In particular, the  
110 depletion of specific high-field-strength elements (HFSEs) (i.e., Zr, Hf, and Ti) and the abundant  
111 abundance of CO<sub>2</sub> in petit-spot basalts imply that their melting sources are related to carbonated

112 materials (Hirano and Machida, 2022; Okumura and Hirano, 2013). ~~Here, the~~ The nature of the  
113 uppermost part of the asthenosphere beneath the oldest Pacific Plate aged 160 Ma was characterized  
114 using the eruptive ages and geochemical properties of six newly observed petit-spot volcanoes and  
115 lava outcrops. We verified the contribution of carbonatitic components and crustal materials to the  
116 melting source of petit-spot volcanoes to understand the nature of the underlying lithosphere–  
117 asthenosphere system and model the geodynamic evolution of the region.

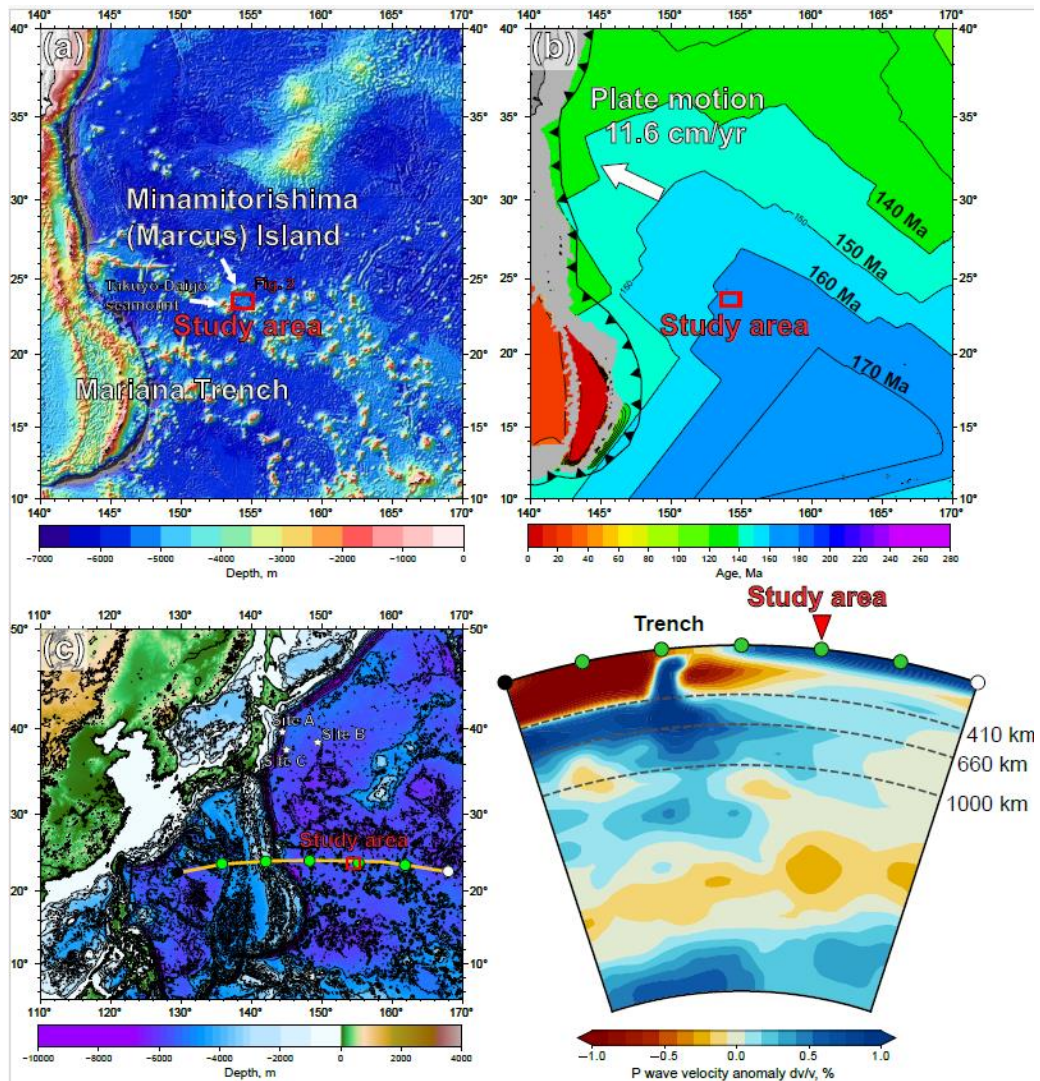
## 119 2 Background

120  
121 ~~In Over~~ the last 20 years, ~~the increasing knowledge~~ there has been an increase in the  
122 ~~understanding~~ of petit-spot volcanic settings, ~~has~~ providing valuable useful insights ~~into~~ on the nature  
123 of the lithosphere–asthenosphere system, ~~especially particularly~~ in the NW Pacific region (Hirano et  
124 al., 2006; Hirano and Machida, 2022). As other implications, subducted petit-spot volcanic fields with  
125 geological disturbances on the seafloor play a role in controlling the hypocentral regions of megathrust  
126 earthquakes (Fujiwara et al., 2007; Fujie et al., 2020; Akizawa et al., 2022). ~~Additionally, and~~ the  
127 vestige of hydrothermal activity ~~due~~ owing to petit-spot magmatism ~~were has~~ recently ~~been~~ reported  
128 (Azami et al., 2023).

129 Petit-spot melts, ~~which originated emerging~~ from the asthenosphere, ~~which are~~ unrelated to  
130 mantle plume, could ~~be a key to elucidating play a crucial role in clarifying~~ the nature of the LAB  
131 (Hirano and Machida, 2022). Their asthenospheric origin was supported by MORB-like noble-gas  
132 isotopic ratios, multi-phase saturation experiment, and geochemistry (Hirano et al., 2006; Hirano and  
133 Machida, 2022; Machida et al., 2015, 2017; Yamamoto et al., 2018). The LAB is ~~recognized identified~~  
134 as a discontinuous transition in seismic velocities at the base of the lithosphere, and its causes are  
135 attributed to hydration, melting, and mineral anisotropy with considerations for the unique  
136 characteristics in each tectonic setting (e.g., Rychert and Shearer, 2009). The occurrence of petit-spot  
137 ~~volcanism~~ ~~volcanoes substantiates confirms~~ the existence of melt at the LAB ~~below beneath~~ the area  
138 at least (Hirano et al., 2006). Recently, similar volcanic activities have been observed ~~worldwide~~  
139 ~~globally~~, including ~~in~~ Java (Sunda) Trench, Tonga Trench, Chile Trench, Mariana Trench, Costa Rica,  
140 North American Basin and Range, and ~~the~~ southern offshore of Greenland, implying the universal  
141 occurrence of petit-spot and similar magmatism (Axen et al., 2018; Buchs et al., 2013; Falloon et al.,  
142 2022; Hirano et al., 2013, 2016, 2019; Reinhard et al., 2019; Taneja et al., 2016; Uenzelmann-Neben  
143 et al., 2012; Yamamoto et al., 2018, 2020; Zhang et al., 2019). Although ~~there is still an open the~~  
144 question of whether the LAB discontinuity is due to the differences in the physical properties of  
145 minerals (e.g., Hirth and Kohlstedt, 1996; Kang and Karato, 2023; Karato and Jung, 1998; Katsura  
146 and Fei, 2021; Stixrude and Lithgow-Bertelloni, 2005; Wang et al., 2006) or the presence of partial  
147 melts ~~remains open~~ (e.g., Audhkhasi and Singh, 2022; Chantel et al., 2016; Conrad et al., 2011;

148 Debayle et al., 2020; Herath et al., 2022; Hua et al., 2023; Kawakatsu et al., 2009; Mierdel et al., 2007;  
149 Sakamaki et al., 2013; Yoshino et al., 2006), the occurrence of petit-spot volcanism ~~reveals-indicates~~  
150 the partial melting of the asthenospheric mantle ~~in~~ the region because they erupted on the seafloor  
151 without hotspot and ridge activities (Hirano et al., 2006; Hirano and Machida, 2022; Machida et al.,  
152 2015, 2017; Yamamoto et al., 2014, 2018, 2020).

153 The petit-spot volcanic province on the abyssal plain of the western Pacific is surrounded by  
154 Cretaceous seamounts and oceanic islands of the Western Pacific Seamount Province (Koppers et al.,  
155 2003) and ~~is~~ located ~~approximately~~ ~~~~~100 km southeast of the Minamitorishima (Marcus) Island (Fig.  
156 1a). The study area corresponds to the oldest portion of the Pacific Plate, aged at 160 Ma, and the foot  
157 of the outer-rise bulge related to the Mariana subduction system (Hirano et al., 2019; Fig. 1b). ~~Such~~  
158 ~~a~~Despite several seamounts crosscutting, subduction-related fore-bulge in front of the Mariana Trench  
159 ~~was detected in satellite gravity maps and~~ has been numerically modeled ~~and detected in satellite~~  
160 ~~gravity maps despite crosscutting by several seamounts~~ (Bellas et al., 2022; Hirano et al., 2019; Zhang  
161 et al., 2014, 2020). ~~The p~~Petrography, geochemistry, and geochronology of petit-spot basalts and  
162 zircons in peperites, ~~which were~~ collected from a knoll, suggested that petit-spot magmas in this region  
163 ascend from the asthenosphere along the concavely flexed plate in response to subduction into the  
164 Mariana Trench at younger than  $\sim$ 3 Ma (Yamamoto et al., 2018; Hirano et al., 2019). Below the study  
165 area, ~~a~~ low seismic velocity zone is observed under the lithosphere (Li et al., 2019; Fig. 1c).  
166 Notwithstanding the low-velocity anomalies crosscutting the lower mantle (Fig. 1c), no active  
167 hotspots (i.e., heat supplies) have been reported around the western Pacific petit-spot province, ~~which~~  
168 ~~is~~ surrounded by Cretaceous Wake seamount chains including Minamitorishima Island and Paleogene  
169 intraplate volcanoes (Koppers et al., 2003; Aftabuzzaman et al., 2021; Hirano et al., 2021). ~~The e~~Qther  
170 petit-spot lava outcrops were observed in a volcanic cluster during three research cruises using the  
171 research vessel (RV) *Yokosuka* (YK16-01, YK18-08, and YK19-05S) with five dives using the  
172 submersible, *Shinkai 6500* (6K#1466, 6K#1521, 6K#1522, 6K#1542, and 6K#1544; Fig. 2); ~~and here~~,  
173 ~~and~~ fresh basalts were collected. ~~The~~ Information ~~of~~ related to the sampling point, depth, ~~and~~  
174 thickness of palagonite rind and manganese-crust ~~as well as, and the~~ age of the western Pacific petit-  
175 spot basalts are provided in Table 1.



176

177 Fig. 1. Geological and geophysical information of the study area. (a) Bathymetry of the western Pacific near the  
 178 Mariana Trench. The red box shows the study area to the southeast of Minamitorishima (Marcus) Island  
 179 (Fig. 2). The bathymetric data are adopted from ETOPO1 (NOAA National Geophysical Data Center;  
 180 <http://www.ngdc.noaa.gov/>). (b) Seafloor age map of the same area as (a). This study area is on a 160–  
 181 170 Ma Pacific Plate, called the Jurassic Quiet Zone (JQZ) (Tivey et al. 2006). The present absolute  
 182 motion of the Pacific Plate and the seafloor age are derived from studies by Gripp and Gordon (1990)  
 183 and Müller et al. (2008), respectively. (c) The cross-section P-wave tomography beneath the thick  
 184 yellow line including the study area on the ETOPO1 bathymetry map (left). The bathymetric images  
 185 were drawn using the Generic Mapping Tool (GMT6: Wessel et al., 2019). The tomographic image  
 186 (right) was drawn using the SubMachine (Hosseini et al., 2018;  
 187 <http://www.earth.ox.ac.uk/~smachine/cgi/index.php> on applying the data of Lu et al. (2019).

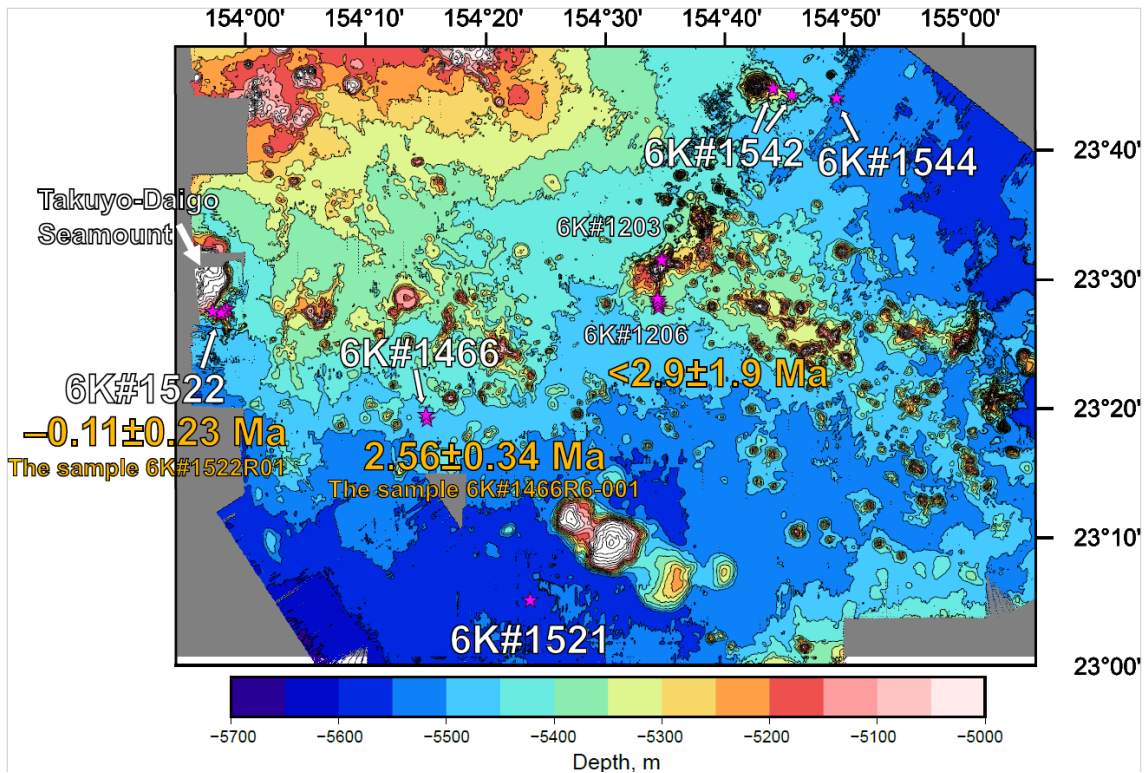
Table. 1  
Information of the collected western Pacific petit-spot basalts

Cruise	Dive	Sample name	Latitude (N)	Longitude (E)	Depth, m	Palagonite rind, mm <sup>*1</sup>	Manganese crust, mm <sup>*1</sup>	Ar-Ar age, Ma
YK16-01	6K#1466	R3-001	23° 19.1009	154° 15.0950	5453	4.45	7.155	
		R3-04	23° 19.1009	154° 15.0950	5453	3.005	5.805	
		R6-001	23° 19.4475	154° 15.0367	5300	6.61	5.205	2.56±0.34
	6K#1521	R7-001	23° 19.4713	154° 15.0000	5267	5.54	4.31	
		R7-003	23° 19.4713	154° 15.0000	5267	-	-	
		R04	23° 5.0880	154° 23.7360	5546	1.045	5.935	
YK18-08	6K#1521	R05	23° 5.0880	154° 23.7360	5546	-	5.625	
		R01	23° 27.6420	153° 58.3140	5300	6.015	5.78	-0.11±0.23 <sup>*2</sup>
		R02	23° 27.6420	153° 58.3140	5300	4.505	2.66	
	6K#1522	R03	23° 27.6420	153° 58.3140	5300	5.44	4.04	
		R05	23° 27.6360	153° 58.3080	5294	2.92	4.785	
		R12	23° 27.4920	153° 58.0620	5189	6.05	5.56	
	6K#1542	R13	23° 27.4920	153° 58.0620	5189	4.545	5.895	
		R14	23° 27.3540	153° 57.8160	5303	2.04	5.475	
		R16	23° 27.4680	153° 57.1200	5182	3.825	3.845	
	6K#1544	R17	23° 27.4680	153° 57.1200	5182	5.19	5.67	
		R03	23° 44.1926	154° 45.6900	5359	3.43	4.26	
		R05	23° 44.1926	154° 45.6900	5359	3.245	4.355	
	6K#1544	R06	23° 44.7064	154° 44.1200	5190	-	-	
		R09	23° 44.7064	154° 44.1200	5190	-	-	
		R04	23° 43.9555	154° 49.4277	5488	4.39	4.955	
		R05	23° 43.9555	154° 49.4277	5488	2.965	4.97	
		R06	23° 43.9555	154° 49.4277	5488	3.425	5.82	

\* 1: The samples which have no data of palagonite and/or Mn-crust thickness are due to the lack of them or crumbled.

\* 2: This is a reference value due to the lack of radiogenic  $^{40}\text{Ar}$  in this sample.

188



189

190 Fig. 2. Detailed bathymetry of the study area. The onboard multibeam data were surveyed during the YK10-05 and  
191 the YK18-08 cruises by the Japan Agency for Marine-Earth Science and Technology (JAMSTEC). The  
192 petit-spot knolls and outcrops were investigated during several dives as 6K#1466, 6K#1521, 6K#1522,  
193 6K#1542, and 6K#1544. The pink-colored stars represent the sampling points. The age information was  
194 obtained in the present study and Hirano et al. (2019). [The bathymetric image was drawn using the GMT](#)  
195 [\(Wessel et al., 2019\).](#)

196

197

198 **3 Field observations, sample locations, and petrography**

199  
200 Here, the eruption~~on~~ve sites of monogenetic volcanoes or lava outcrops are approximately ~~along~~  
201 ~~aligned with~~ each dive site numbered 6K#1466, #1521, #1522, #1542, and #1544 conducted using the  
202 *Shinkai 6500*. ~~Only~~The 6K#1466 dive was conducted at two types of monogenetic volcanoes, ~~divided~~  
203 ~~into~~categorized as the glassy type (R3) and crystalline; ~~and~~ vesicular type (R6 and R7)~~-types~~ based on  
204 the geochemical and petrographic descriptions and occurrence of basaltic samples.

205  
206 **3.1 YK16-01 cruise and 6K#1466 dive**

207  
208 During the YK16-01 cruise, a small conical knoll (ca. 0.04 km<sup>3</sup>) was investigated by a  
209 submersible dive, 6K#1466 (Figs. 2 and 3a). The lava flows, which were observed in a hollow lava  
210 tube resulting in sediment-rolling/disturbing eruption, were located ~~approximately~~~600 m south of  
211 the top of the knoll~~-, featuring~~ extremely fresh and glassy samples; (6K#1466R3-001 and R3-004  
212 basalts) (Fig. 3a). Vesicular pillow basalts were collected on the western slope of the knoll (samples  
213 6K#1466R6-001, R7-001, and R7-003; Fig. 3a). ~~Although only~~While the strong acoustic reflection  
214 could not ~~completely~~entirely distinguish the petit-spot lava fields in ferromanganese nodule fields,  
215 ~~this the 6K#1466~~ dive revealed lava outcrops using a sub-bottom profiler (SBP) and a multi-narrow-  
216 beam echo sounder (MBES). In detailSpecifically, the petit-spot lava field, as an acoustically opaque  
217 layer, ~~was identified by~~exhibited a vigorous backscattering intensity in the MBES, along with the  
218 distributions of the basement and sediment layers in the SBP.

219 The 6K#1466R3-001 and R3-004 samples were extremely fresh glassy basalts. The ~~R3-001 and~~  
220 ~~R3-004 basaltssamples~~ exhibited similar petrographic features (Fig. 3a). These ~~basalts samples~~ were  
221 ~~covered enveloped~~ by a 3.0–4.5-mm-thick palagonite layer (hydrated quenched glass), ~~and with~~ their  
222 outermost parts ~~were being~~ surrounded by a 5.8–7.2-mm-thick ferromanganese crust (Fig. 3a). They  
223 were less vesicular (<3 vol.%) and were dominantly composed of basaltic glass, ~~with~~ euhedral–  
224 subhedral olivine microphenocrysts (~100–500 µm in size), ferrotitanium oxide (<50 µm in size), and  
225 minor plagioclase (~500 µm in size) (Fig. 3a). ~~Secondary~~No ~~secondary~~ phases such as(e.g., clay  
226 minerals) were ~~not~~observed.

227 The 6K#1466R6-001, R7-001, and R7-003 basalts, which were covered with a 4.3–5.2-mm-  
228 thick ferromanganese crust over 5.5–6.6-mm-thick palagonite rinds, exhibited high vesicularity (20–  
229 40 vol.%) (Fig. 3a). Mikuni et al. (2022) reported ~~c~~ertain pyroxene-dominated xenocrysts and  
230 peridotite xenoliths ~~have been reported by~~ Mikuni et al. (2022). The basaltic groundmass was  
231 ~~characterized by~~comprised needle-shaped clinopyroxene (50–400 µm in size), subhedral olivine partly  
232 with aureoles of iddingsite (up to 100 µm in size), ferrotitanium oxide, minor spinel (up to 10 µm in  
233 size), glass, and crystallite, notably without remarkable phenocrysts (Fig. 3a). The photomicrograph

234 of R6-001 is shown in Fig. 3a.

235

### 236 3.2 YK18-08 cruise and 6K#1521 and **6K#1522** dives

237

238 Two submersible dives (6K#1521 and **#1522**) were conducted during the YK18-08 cruise to  
239 investigate petit-spot volcanoes. During the 6K#1521 dive, a small lava outcrop was **discovered**  
240 **identified** in the abyssal plain by tracing **at the** strong acoustic reflection, which was expectedly **to**  
241 **originated****derived** from intrusive rock bodies, in the sedimentary layer detected by deep-sea SBP  
242 equipped on the *Shinkai 6500*. **T****We observed that** the strong reflective surface gradually became  
243 shallow during the navigation, revealing the small lava outcrop (Figs. 2 and 3b). Fresh and massive  
244 (nonvesicular) basalts were collected from this outcrop (samples 6K#1521R04 and R05; Fig. 3b). The  
245 samples **obtained** from the 6K#1522 dive at a seamount exhibited highly irregular shapes, and massive  
246 lava flows, pillows, and lava breccia were observed (Fig. 3c). All the samples were fresh vesicular  
247 basalts (6K#1522R01, R02, R05, R12, R13, R16, and R17; Fig. 3c).

248 The fresh, massive, and nonvesicular basalts were **collected during the obtained by** 6K#1521  
249 dive (R04 and R05) **and** comprised euhedral olivine microphenocrysts (150–400  $\mu\text{m}$  in size), two types  
250 of ferrotitanium oxide (50–150  $\mu\text{m}$  in size), and crystallite (Fig. 2b). Secondary phases were not  
251 observed **as well**. They were covered with **a** 5.6–5.9–mm-thick ferromanganese crust and  $\sim$ 1.0–mm-  
252 thick palagonite rinds (Fig. 3b), **however, but** R05 did not have palagonite rinds. The photomicrograph  
253 of R04 is shown in Fig. 3b.

254 The seven fresh basalts collected during the 6K#1522 dive (6K#1522R01, R02, R05, R12, R13,  
255 R16, and R17), exhibited high vesicularity (20–40 vol.%) with 2.9–6.0–mm-thick palagonite rinds  
256 covered with 2.7–5.9–mm-thick ferromanganese crusts (Fig. 3c). Euhedral–subhedral olivine  
257 microphenocrysts (glomeroporphyritic, 30–200  $\mu\text{m}$  in size), radial–needle-shaped clinopyroxene,  
258 iddingsite (<200  $\mu\text{m}$  in size), spinel, and glass with minor xenocrystic olivines were observed (Fig.  
259 3c). The photomicrograph of R01 is shown in Fig. 3c.

260

### 261 3.3 YK19-05S cruise and 6K#1542 and **6K#1544** dives

262

263 A petit-spot knoll and **related****associated** lava flows were **surveyed****investigated** by the 6K#1542  
264 and #1544 dives, **respectively**, during the YK19-05S cruise (Fig. 2). During the 6K#1542 dive,  
265 geological survey and rock sampling were conducted from two points on the eastern slope of the knoll  
266 (Figs. 2 and 3d). **H****e****r****e**, **t****T****he** 6K#1542R03 and R05 basalts were collected from the lava-breccia field  
267 covered with **a** thin ferromanganese crust (Fig. 3d). **A****d****d****ditionally**, **s****S****amples** R06 and R09 were  
268 obtained from the lobate-surface lava between tubular lavas closer to the summit than R03 and R05  
269 (Fig. 3d).

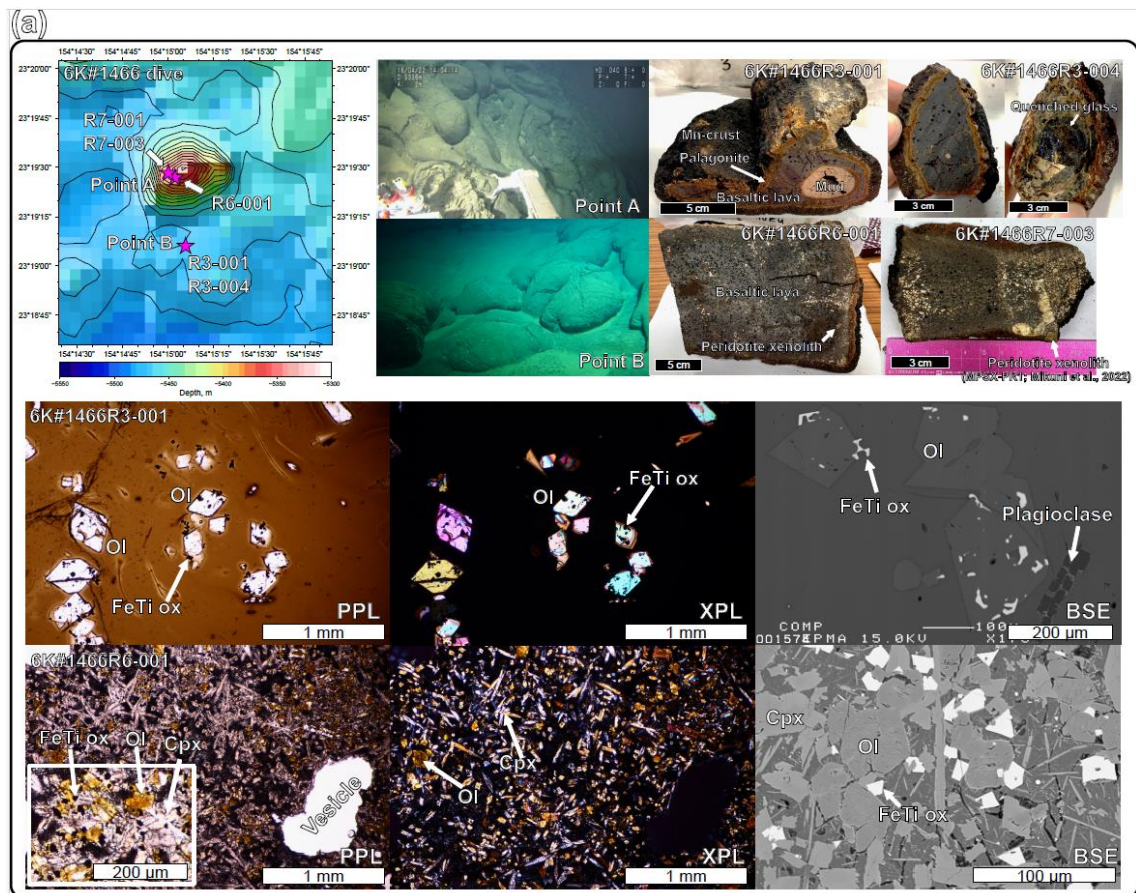
270        High-resolution (one-meter scale) bathymetric mapping was successfully conducted during the  
271        6K#1544 dive, ~~and this which~~ can contribute to future oceanographic investigations using ~~the a Human~~  
272        ~~human-occupied vehicle~~ (Kaneko et al., 2022). ~~During this acoustic survey, several~~ mounds, 10–  
273        20 m in height and a few hundred meters in diameter, were recognized ~~during this acoustic survey~~  
274        (Fig. 3d). We observed these mounds and collected samples from outcrops during the second half of  
275        the dive. ~~Furthermore, pillow lavas, tumuli, and lava breccias were observed, and basaltic samples~~  
276        (6K#1544R04, R05, and R06) were collected (Fig. 3d).

277        Four vesicular basalts (10–30 vol.% vesicularity; 6K#1542R03, R05, R06, and R09) were  
278        covered with 4.3–4.4-mm-thick ferromanganese crusts. The outer palagonitic rinds were 3.2–3.4-mm  
279        thick (Fig. 3d). ~~A few to 300 µm-sized euhedral–subhedral olivine microlites (up to sizes of 300~~  
280        ~~µm)~~ and microphenocrysts were glomeroporphyritic (Fig. 3d). The groundmass was dominated by  
281        needle dendritic clinopyroxenes (~100 µm in size). ~~The others were, along with~~ olivine, spinel, glass,  
282        and xenocrystic olivine megacrysts. The photomicrograph of R06 is shown in Fig. 3d.

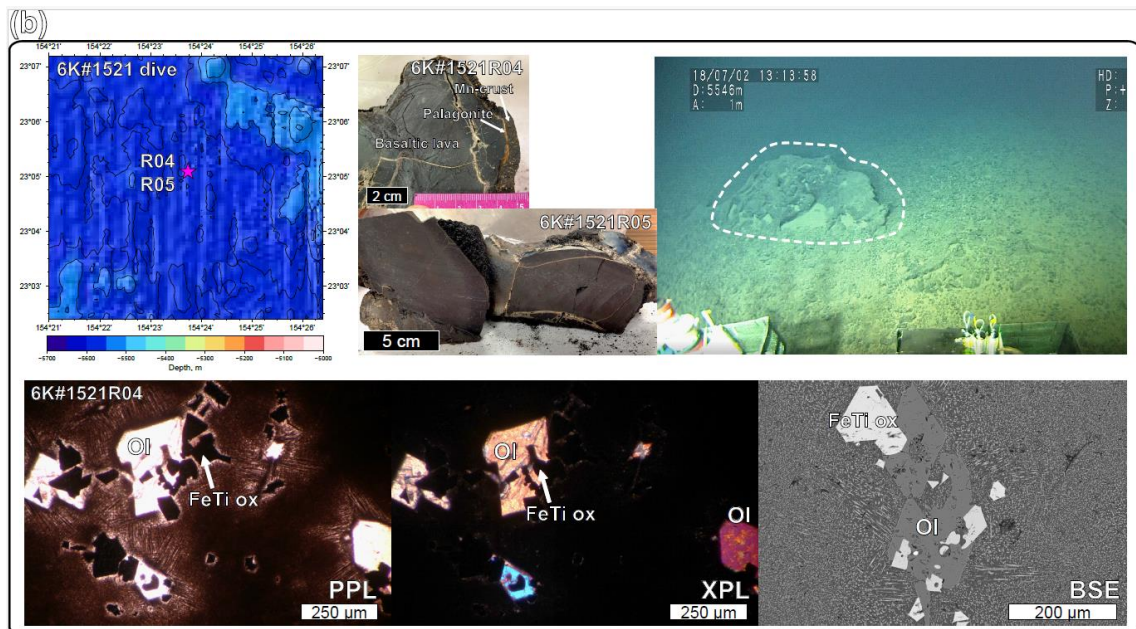
283        ~~The b~~ Basaltic samples from the 6K#1544 dive (6K#1544R04, R05, and R06) were covered with  
284        ferromanganese crust (5.0–5.8-mm-thick) over palagonitic rinds (3.4–4.4-mm-thick). All the  
285        samples exhibited high vesicularity in the range of 20–35 vol.% (Fig. 3d). They comprised olivine  
286        microphenocrysts (30–250 µm in size, euhedral–subhedral or columnar), clinopyroxene (<100 µm,  
287        needle, columnar, radial or dendritic shape), spinel, and glass without secondary phases (Fig. 3d).

288        The photomicrograph of R04 is shown in Fig. 3d. During macroscopic observations, practically  
289        all the basalts from the 6K#1542 and 6K#1544 dives exhibited similar vesicularity and freshness.  
290        Their geochemical features were also similar to each other and are described in Sect. 5-1 and 5-2.

291

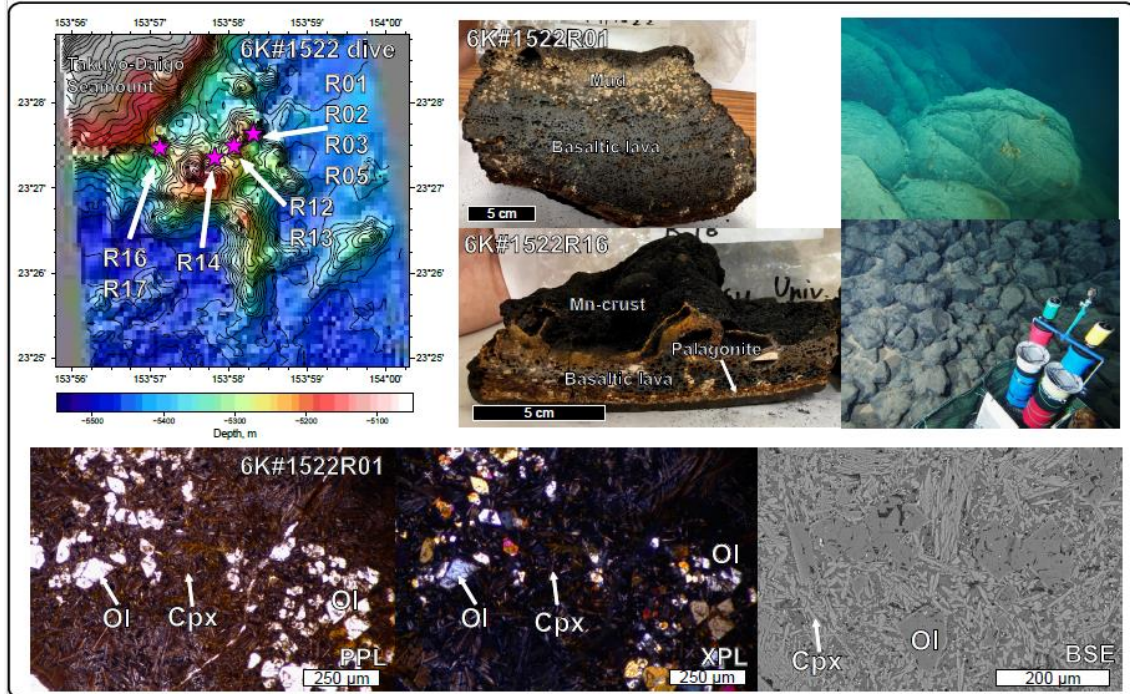


292

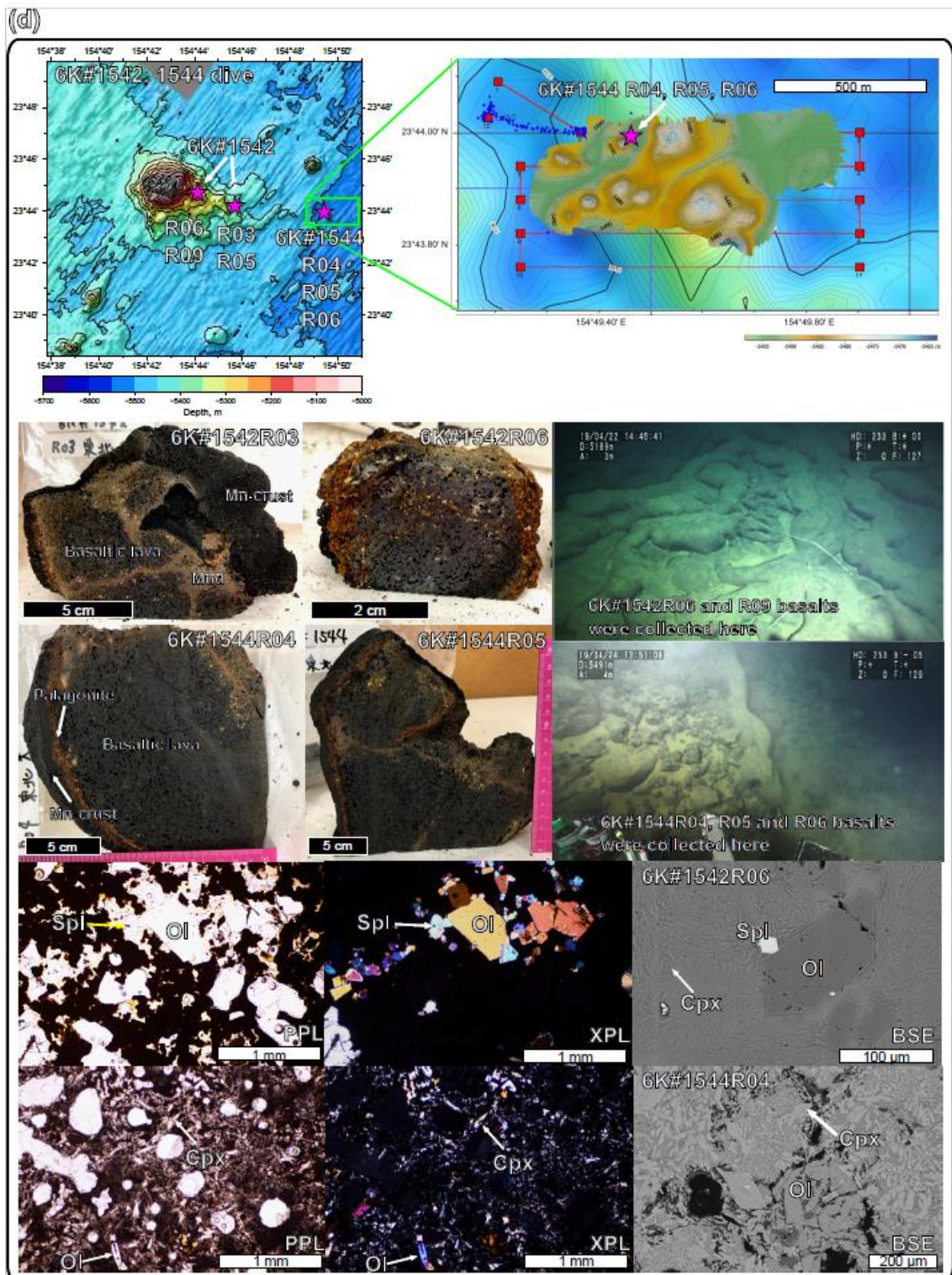


293

(C)



294



295

296 Fig. 3. Bathymetric map with photos of the outcrop, the collected samples, and their photomicrographs with detailed  
 297 bathymetry of the sampling points. (a) The 6K#1466, (b) 6K#1521, (c) 6K#1522, and (d) 6K#1542 and  
 298 6K#1544 dives using the *Shinkai* 6500 by JAMSTEC. The 1-m gridded bathymetry of the 6K#1544 dive  
 299 is shown in (d), obtained using an MBES equipped with the *Shinkai* 6500 over a 100-m resolution map

300 obtained using the surface ship, R/V *Yokosuka* (Kaneko et al., 2022). The photomicrographs of  
301 representative samples are shown for plane-polarized light (PPL), cross-polarized light (XPL), and  
302 backscatter electron (BSE). Ol, olivine; Cpx, clinopyroxene; Mgt, magnetite; Spl, spinel. [The bathymetric](#)  
303 [images were drawn using the GMT \(Wessel et al., 2019\).](#)

304

305

306 **4. Analytical methods**

307

308 **4.1 Major and trace element analysis of volcanic glass, mineral, and whole-rock**

309

310 Major element compositions of glasses and minerals were determined using an electron probe  
311 micro analyzer (EPMA). JXA-8900R at Atmosphere and Ocean Research Institute (AORI), the  
312 University of Tokyo was used for glass analysis and JXA-iHP200F at GSJ, AIST was used for mineral  
313 analysis. The analyses were performed using an accelerating voltage of 15 kV, a beam current of 12  
314 nA, and a beam diameter of 10  $\mu\text{m}$  for glass and 2  $\mu\text{m}$  for mineral. A peak counting time of 20 s and  
315 a background counting time of 10 s were used, except for Ni, for which a peak counting time of 30 s  
316 and a background counting time of 15 s. For Na analysis of glass, the peak counting time was 5 s and  
317 the background counting time was 2 s. Natural and synthetic minerals were used as standards, and data  
318 were corrected using a ZAF online correction program (Akizawa et al., 2021). Major element  
319 composition of glass was determined by the mean value of 10 analytical points.

320 Trace element compositions of minerals were determined using a laser ablation-inductively  
321 coupled plasma-mass spectrometry (LA-ICP-MS; New Wave Research UP-213 and Agilent 7500s)  
322 at Kanazawa University. The Nd: YAG deep UV (ultraviolet) laser's wavelength is 213 nm. The  
323 analyses were conducted with 100  $\mu\text{m}$  spot size. A repetition frequency of 6 Hz and a laser energy  
324 density of 8 J  $\text{cm}^{-2}$  were used. NIST612 glass (distributed by National Institute of Standards and  
325 Technology) was employed for calibration, using the preferred values of Pearce et al. (1997). Data  
326 reduction was undertaken with  $^{29}\text{Si}$  as the initial standard, and  $\text{SiO}_2$  concentrations were obtained by  
327 an electron microprobe analysis (Longerich et al., 1996). BCR-2G (distributed by the United States  
328 Geological Survey) was used as a secondary standard to assess the precision of each analytical  
329 session (Jochum and Nohl, 2008).

330 Whole-rock major and trace element compositions of rock samples were analyzed by Activation  
331 Laboratories Ltd., Canada, using Code 4Lithoresearch Lithogeochemistry and ultratrace5 Exploration  
332 Geochemistry Package. The former package uses lithium metaborate/tetraborate fusion with  
333 inductively coupled plasma optical emission spectrometry (FUS-ICP-OES) and inductively coupled  
334 plasma mass spectroscopy (FUS-ICP-MS) for the major and trace element analyses, respectively. The  
335 latter package uses inductively coupled plasma optical emission spectrometry (ICP-OES) and

336 inductively coupled plasma mass spectroscopy (ICP-MS) for the major and trace element analyses,  
337 respectively.

339 **4.2 Sr, Nd, and Pb isotope analysis**

340 **4.2.1 Acid leaching**

343 Acid leaching was conducted for the selected basaltic samples on the basis of the procedure of  
344 Weis and Frey (1991, 1996) as follows: [1] About 0.3–0.4 or 0.6 g of rock powder is weighed into an  
345 acid-washed 15 mL Teflon vial (Savilex®). [2] 10 or 12 mL of 6N (N: normality) HCl were added, and  
346 then heated at 80°C for 20–30 min. [3] After heating, the suspension is ultra-sonicated in 60°C water  
347 for 20 min. [4] The supernatant is decanted. Steps [2] to [4] were repeated more than 4 times (up to 6  
348 times) until the supernatant become clear or pale yellow to colorless. [5] TAMAPURE-AA Ultrapure  
349 water (Tama Chemicals; Co., Ltd.), which includes a lower Pb blank than milli-Q H<sub>2</sub>O, were added  
350 instead of 6N HCl, and the suspension is ultra-sonicated for 20 min. This step is conducted twice. [6]  
351 The leached rock powder is dried on a hot plate at 120°C. [7] After cooling, the powder is weighed.

353 **4.2.2 Extraction of Pb, Sr, and Nd**

355 The extraction of Pb, Sr, and Nd was performed following the procedures of Tanimizu and  
356 Ishikawa (2006) and Machida et al. (2009). First, from ~50 to ~100 mg of rock powder was weighted  
357 in a 7 mL Teflon vial (designated as “vial A”), and digested using mixed acid composed of HF and  
358 HBr. The separation was conducted by cation exchange resin (AG-1X8; Bio-Rad Laboratories Inc.)  
359 on the basis of procedures described in Tanimizu and ishikawa (2006). All fractions from the first and  
360 second supernatant loading (0.5 M HBr) to the elution of other elements (mixed acid composed of  
361 0.25 M HBr and 0.5 M HNO<sub>3</sub>) were collected in another 7 mL Teflon vial (designated as “vial B”) for  
362 Sr and Nd separation. Finally, Pb was extracted by 1 mL of 1M HNO<sub>3</sub> in another 7 mL Teflon vial  
363 (designated as “vial C”). The procedural blanks for Pb totaled less than 23 pg.

364 The Sr and Nd-bearing solution in the vial B was transferred into the vial A containing residues  
365 of digested samples. 2 mL of HClO<sub>4</sub> and 2 mL HNO<sub>3</sub> was further added to the vial A, and the residue  
366 was dissolved at 110 °C. Both Sr and Nd were separated by column with a cation exchange resin  
367 (AG50W-8X; Bio-Rad Laboratories Inc.) and a Ln resin (Eichrom Technologies Inc.) on the basis of  
368 procedures described in Machida et al. (2009). The separated Sr and Nd were further purified by  
369 column separation with a cation exchange resin. The total procedural blanks for Sr and Nd were less  
370 than 100 pg.

372 **4.2.3 Analytical procedure**

373

374 Pb isotopic ratios were obtained using the multi-collector ICP-MS (MC-ICP-MS; Neptune plus,  
375 Thermo Fisher Scientific), with nine Faraday collectors, at Chiba Institute of Technology (CIT), Japan.  
376 The NIST SRM-981 Pb standard was also analyzed and yielded the average values of  $^{206}\text{Pb}/^{204}\text{Pb} =$   
377  $16.9303 \pm 0.0005$ ,  $^{207}\text{Pb}/^{204}\text{Pb} = 15.4828 \pm 0.0006$ , and  $^{208}\text{Pb}/^{204}\text{Pb} = 36.6710 \pm 0.0016$ . These  
378 correspond to previous values determined using MC-ICP-MS with Tl normalization, but they were  
379 slightly lower than values determined by TIMS in Tanimizu and Ishikawa (2006) from the  $^{207}\text{Pb}$ - $^{204}\text{Pb}$   
380 double-spike. Reproducibility was monitored by an analyses of the JB-2 GSJ standard, and the  
381 obtained values were  $^{206}\text{Pb}/^{204}\text{Pb} = 18.3326 \pm 0.0005$ ,  $^{207}\text{Pb}/^{204}\text{Pb} = 15.5453 \pm 0.0006$ , and  $^{208}\text{Pb}/^{204}\text{Pb}$   
382 =  $38.2240 \pm 0.0017$ .

383 Sr and Nd isotopic analyses for powdered rocks and glasses were conducted using the thermal  
384 ionization mass spectrometry (TIMS; Triton XT, Thermo Fisher Scientific) with nine Faraday  
385 collectors, at CIT. 1.5  $\mu\text{L}$  of 2.5M HCl and 0.5M HNO<sub>3</sub> was used for loading of separated Sr and Nd  
386 of sample on the single and double Re-filament, respectively. The measured isotopic ratios were  
387 corrected for instrumental fractionation by adopting the  $^{86}\text{Sr}/^{85}\text{Sr}$  value to be 0.1194 and that of  
388  $^{146}\text{Nd}/^{144}\text{Nd}$  to be 0.7219. The average value for the NIST SRM-987 Sr standard was 0.710239  
389  $\pm 0.000005$  (2 $\sigma$ , n = 2), and that for the GSJ JNd-1 Nd standard was  $0.512103 \pm 0.000005$  (2 $\sigma$ , n = 2).  
390 They agree well with values from the literature for the NIST SRM-987 ( $^{87}\text{Sr}/^{86}\text{Sr} = 0.710252 -$   
391 0.710256; Weis et al., 2006) and JNd-1 ( $^{143}\text{Nd}/^{144}\text{Nd} = 0.512101$ ; Wakaki et al., 2007). Consequently,  
392 we did not correct the values of the unknowns for offsets between the measurements and the values  
393 for the Sr and Nd standards.

394

395 **4.3  $^{40}\text{Ar}/^{39}\text{Ar}$  dating**

396

397 Samples for  $^{40}\text{Ar}/^{39}\text{Ar}$  dating were prepared by separating crystalline groundmass after crushing  
398 them to sizes between 100 and 500  $\mu\text{m}$ . The separated groundmass samples were leached by HNO<sub>3</sub> (1  
399 mol/L) for one hour to remove clays and altered materials. All samples were wrapped in aluminum  
400 foil along with JG-1 biotite (Iwata, 1998), K<sub>2</sub>SO<sub>4</sub>, and CaF<sub>2</sub> flux monitors. Any amorphous (e.g.,  
401 quenched glass) was removed because  $^{39}\text{Ar}$  may move from one phase to another in a process known  
402 as “recoil.” This can create a disturbed age spectrum when  $^{39}\text{Ar}$  is produced from  $^{39}\text{K}$  in amorphous  
403 material through interaction with fast neutrons during irradiation of the sample. Samples were  
404 irradiated for 6.6 days in the Kyoto University Research Reactor (KUR), Kyoto University. Argon  
405 extraction and isotopic analyses were undertaken at the Graduate School of Arts and Sciences, the  
406 University of Tokyo. The sample gases were extracted by incremental heating of 10 or 11 steps  
407 between 600°C and 1500°C. The analytical methods used are the same as those used by Ebisawa et al.

408 (2004) and Kobayashi et al. (2021).

409

410 **5 Results**

411

412 To describe the geochemical and chronological results, each sample group was denoted by its  
413 dive number, e.g., the sample group obtained from the 6K#1521 dive was labeled “1521 samples or  
414 basalts”. The basalts from the 6K#1466 dive were divided into two groups for R3 (collected from the  
415 seafloor south of the knoll) and R6–R7 (sampled on the knoll) based on their geographical,  
416 petrological, and compositional differences. The mineral compositions of each petit-spot basalt are  
417 shown in Fig. S1 and Table S1, S2 and S3.

418

419 **5.1 Major and trace element compositions**

420

421 The major and trace element compositions for the whole rock and glass of the petit-spot basalts  
422 are listed in Table 2 and 3, respectively. The basalt compositions for a petit-spot knoll were reported  
423 by Hirano et al. (2019) (expressed as “1203, 1206” in each figure). The data are discussed along with  
424 the reported NW Pacific petit-spots (Hirano and Machida, 2022). Using a total alkali vs. silica (TAS)  
425 diagram, virtually all the samples were classified as alkalic rocks, but the 1542 and 1544 basalts were  
426 plotted near the boundary between alkalic and non-alkalic (Fig. 4a). Two petit-spot basalts (1466R7-  
427 001 and R7-003) from the petit-spot knoll were notably silica-undersaturated (i.e.,  $\text{SiO}_2 = 39.3\text{--}39.4$   
428 wt%) and classified as foidite (Mikuni et al., 2022). All the western Pacific petit-spot basalts, except  
429 for the ~~6K~~#1466R7 basalts, were sodic ( $\text{K}_2\text{O}/\text{Na}_2\text{O} = 0.24\text{--}0.58$ ) and were notably discriminated to  
430 the potassic NW Pacific petit-spots (Fig. 4b).

431 Selected major element oxides and trace element ratios vs.  $\text{MgO}$  plots for the petit-spot basalts  
432 are shown in Figs. 5 and 6, respectively. The  $\text{MgO}$  concentrations of the 1466R3 and 1521 samples  
433 each exhibiting similar petrographic features (i.e., nonvesicular, and glassy) were characterized by  
434 values (4.0–4.4 wt%) lower than those of other vesicular samples (6.6–9.3 wt%). The  $\text{K}_2\text{O}$ ,  $\text{Na}_2\text{O}$ ,  
435  $\text{Al}_2\text{O}_3$ , and  $\text{SiO}_2$  contents negatively correlated with  $\text{MgO}$  (Figs. 5a–d). The  $\text{CaO}$ ,  $\text{FeO}_{\text{T}}$ , and  
436  $\text{CaO}/\text{Al}_2\text{O}_3$  abundances exhibited positive correlations with  $\text{MgO}$  (Figs. 5e–g). The  $\text{TiO}_2$   
437 concentrations exhibited no correlations with  $\text{MgO}$  (Fig. 5h), as well as the selected trace element  
438 ratios (Figs. 6a–g) except for the  $\text{Sm}/\text{Hf}$  ratio with positive correlations (Fig. 6h). The  $\text{Sm}/\text{Hf}$  ratio also  
439 negatively correlated with  $\text{SiO}_2$  (Fig. S2). The study samples exhibited whole-rock loss on ignition  
440 (LOI) in the range of 0.67–1.72 wt%, excluding two relatively altered samples, ~~6K~~#1466R7-001 (LOI  
441 = 2.68 wt%) and R7-003 basalts (LOI = 6.29 wt%).

442 The PM-normalized (Sun and McDonough, 1989) trace element patterns for the petit-spot  
443 basalts, including those reported by a previous study (Hirano et al., 2019), were shown for each dive

444 compared to the representative ocean island basalt (OIB) in Figs. 7a–f. The petit-spot basalts generally  
 445 showed high light rare earth element (LREE)/heavy REE (HREE) ratios. Negative Zr, Hf, Ti, and Y  
 446 anomalies were commonly observed in these western Pacific petit-spots as well as those of the NW  
 447 Pacific petit-spots (Fig. 7g). The 1466 basalts collected on the seafloor south of the knoll (6K#1466R3-  
 448 001 and [1466R3-004 basalts](#)) were compositionally different from those obtained on the knoll  
 449 ([6K#1466R7-001 and- 1466R7-003 samples](#)). The basalts from the 6K#1542 and #1544 dives,  
 450 collected from nearby locations, had the same compositions in major and trace element ratios in both  
 451 whole rock and glass, respectively (Figs. 4, 5, 6, 7e, and f). These samples in the Ba/Nb and Sm/Hf  
 452 diagrams were plotted in the range of “Group 3” in the discrimination of the NW Pacific petit-spot  
 453 basalts (Machida et al., 2015), indicating their negative Zr and Hf anomalies without notable U, Th,  
 454 Nb, and Ta anomalies in the PM-normalized trace element patterns (Fig. 7h). The Sm/Hf ratio of the  
 455 differentiated 1466R3 samples was lower than that of other samples. A positive correlation between  
 456 fluid mobile and immobile elements, Ba vs. Nb (Fig. 8a) and U vs. Th (Fig. 8b), respectively, was  
 457 observed, excluding the Ba of the 1466R7 samples (Fig. 8a).  
 458

Table. 2  
 Major and trace element compositions of western Pacific petit-spot basalts.

Cruise	YK16-01				YK16-01				YK16-01				YK16-08				YK16-08				YK16-08					
	Sample name	6K#1466R3-001	6K#1466R3-004	6K#1466R7-001	6K#1466R7-003	6K#1542R04	6K#1542R05	6K#1522R01	6K#1522R01	6K#1522R01	6K#1522R02	6K#1522R02	6K#1522R02	6K#1522R02	6K#1522R02	6K#1522R04	6K#1522R05	6K#1522R06	6K#1522R06	6K#1522R06	6K#1542R04	6K#1542R05	6K#1542R06	6K#1542R12		
Sample type	Glass	Glass	Glass	Whole rock	Glass	Glass	Glass	Glass	Glass	Glass	Glass	Glass	Glass	Glass	Glass	Glass	Glass	Glass	Glass	Glass	Glass	Glass	Glass			
Method	EPMA	EPMA	EPMA	EPMA	EPMA	EPMA	EPMA	EPMA	EPMA	EPMA	EPMA	EPMA	EPMA	EPMA	EPMA	EPMA	EPMA	EPMA	EPMA	EPMA	EPMA	EPMA	EPMA			
mean of n=10	2 $\sigma$		mean of n=10	2 $\sigma$		mean of n=10	2 $\sigma$		mean of n=10	2 $\sigma$		mean of n=10	2 $\sigma$		mean of n=10	2 $\sigma$		mean of n=10	2 $\sigma$		mean of n=10	2 $\sigma$		mean of n=10	2 $\sigma$	
wt%																										
SiO <sub>2</sub>	51.56	0.93	50.63	0.79	39.40	39.27	48.42	0.36	46.78	0.97	45.92	1.40	45.28	45.90	0.79	45.38	1.56	46.02	0.69	46.02	0.69	46.02	0.69	46.02	0.69	
TiO <sub>2</sub>	2.31	0.20	2.19	0.22	3.82	3.68	3.65	0.30	3.32	0.25	2.37	0.17	2.43	2.51	0.20	2.33	0.13	2.45	0.21	2.45	0.21	2.45	0.21	2.45	0.21	
Al <sub>2</sub> O <sub>3</sub>	14.99	0.57	15.10	0.37	11.41	11.46	15.12	0.31	14.38	0.45	12.74	0.23	12.48	12.82	0.25	11.99	0.53	12.91	0.14	12.91	0.14	12.91	0.14	12.91	0.14	
Cr <sub>2</sub> O <sub>3</sub>	-	-	-	-	0.03	0.03	-	-	-	0.01	0.05	0.03	0.02	0.05	0.01	0.05	0.02	0.05	0.01	0.05	0.02	0.05	0.01	0.05	0.02	
FeO <sup>+</sup>	9.68	0.30	9.17	0.62	15.12	14.90	10.65	0.29	9.77	0.79	11.72	0.16	12.32	11.64	0.42	10.77	1.02	11.62	0.24	11.62	0.24	11.62	0.24	11.62	0.24	
MnO	0.14	0.04	0.14	0.05	0.21	0.20	0.16	0.04	0.14	0.03	0.18	0.04	0.18	0.16	0.04	0.15	0.05	0.17	0.05	0.17	0.05	0.17	0.05	0.17	0.05	
MgO	4.04	0.11	3.99	0.11	9.34	7.66	4.43	0.08	4.36	0.10	7.36	0.17	7.26	7.33	0.10	7.12	0.23	7.14	0.16	7.14	0.16	7.14	0.16	7.14	0.16	
CaO	7.71	0.11	7.41	0.25	11.19	10.02	8.34	0.68	7.80	0.29	10.72	0.14	11.18	10.81	0.22	10.33	0.68	10.79	0.10	10.79	0.10	10.79	0.10	10.79	0.10	
Na <sub>2</sub> O	4.61	0.24	4.38	0.50	2.15	2.29	3.84	0.31	4.05	0.55	4.16	0.21	3.53	4.16	0.29	4.16	0.24	4.01	0.46	4.01	0.46	4.01	0.46	4.01	0.46	
K <sub>2</sub> O	2.31	0.08	2.24	0.12	1.65	2.08	2.25	0.27	2.13	0.12	1.38	0.06	1.42	1.40	0.13	1.31	0.10	1.38	0.04	1.38	0.04	1.38	0.04	1.38	0.04	
NiO	0.01	0.03	0.01	0.03	0.03	0.02	-	0.04	-	0.05	0.02	0.03	0.02	0.04	0.01	0.04	0.02	0.04	0.02	0.04	0.02	0.04	0.02	0.04	0.02	
P <sub>2</sub> O <sub>5</sub>	0.93	0.03	0.91	0.06	1.08	1.12	1.53	0.11	1.51	0.03	0.80	0.06	0.83	0.80	0.08	0.80	0.08	0.82	0.06	0.82	0.06	0.82	0.06	0.82	0.06	
Total	98.28	-	96.16	-	99.10	98.38	94.24	-	97.35	-	98.67	-	97.56	94.40	-	97.31	-	97.56	-	97.56	-	97.56	-	97.56	-	
Mg#	42.64	-	43.68	-	52.42	47.82	42.57	-	44.33	-	52.83	-	51.24	52.89	-	54.11	-	52.28	-	52.28	-	52.28	-	52.28	-	
LOI	-	-	-	-	2.68	6.29	-	-	-	-	-	-	-	-	1.72	-	-	-	-	-	-	-	-	-	-	

FeO<sup>+</sup> as total values.

Mg# = 100 × Mg / [Mg+Fe<sup>2+</sup>]<sub>total</sub>.

- -: not detected

\*: Analyzed by ActiLab

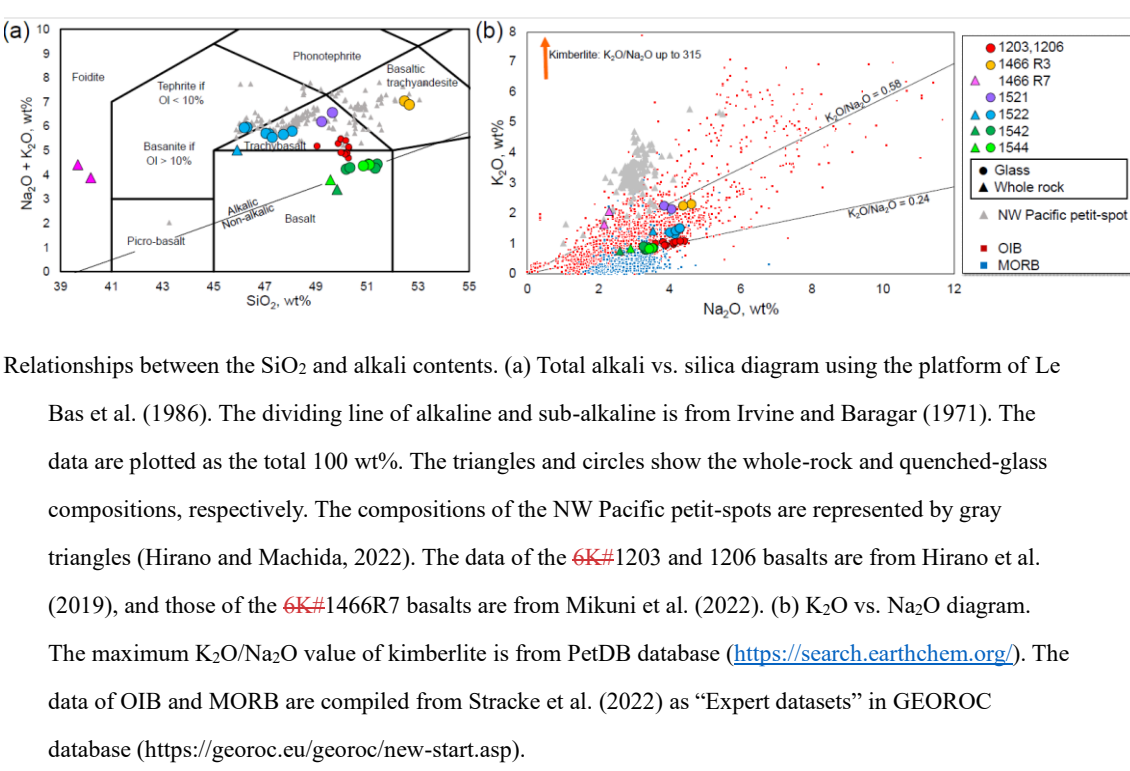
Table. 2 continued

YK18-08	YK18-08				YK18-08				YK18-08				YK18-08				YK18-08				YK18-08						
	6K#1522R13	6K#1522R16	6K#1522R17	6K#1542R03	6K#1542R03	6K#1542R05	6K#1542R06	6K#1542R06	6K#1542R09	6K#1542R09	6K#1542R09	6K#1542R04	6K#1542R04	6K#1542R04	6K#1542R04	6K#1542R05	6K#1542R05	6K#1542R06	6K#1542R06	6K#1542R06	6K#1542R06	6K#1542R06	6K#1542R06	6K#1542R06			
Sample type	Glass	Glass	Glass																								
Method	EPMA	EPMA	EPMA																								
mean of n=10	2 $\sigma$		mean of n=10	2 $\sigma$		mean of n=10	2 $\sigma$		mean of n=10	2 $\sigma$		mean of n=10	2 $\sigma$		mean of n=10	2 $\sigma$		mean of n=10	2 $\sigma$		mean of n=10	2 $\sigma$		mean of n=10	2 $\sigma$		
47.09	0.68	45.22	0.73	45.06	0.98	48.66	1.14	49.35	1.51	49.66	1.11	50.09	0.93	50.54	0.43	49.08	50.53	0.61	49.59	1.18	50.53	0.61	49.59	1.18			
2.50	2.20	2.58	0.20	2.67	0.27	2.11	0.19	2.16	2.13	0.18	2.25	0.22	2.24	0.20	2.04	0.23	2.13	2.08	0.25	2.07	0.24	2.08	0.25	2.07	0.24		
13.08	0.33	12.55	0.17	12.55	0.14	13.49	0.18	12.52	13.38	0.19	12.55	0.43	12.78	0.33	13.18	0.12	13.25	12.94	0.34	12.94	0.36	12.94	0.36	12.94	0.36		
0.02	0.05	0.04	0.04	0.02	0.06	0.04	0.05	0.05	0.03	0.07	0.02	0.04	0.04	0.04	0.03	0.05	0.03	0.05	0.03	0.05	0.03	0.05	0.03	0.05	0.03		
1.74	0.49	11.94	0.40	10.66	0.66	10.66	0.00	11.40	10.47	0.25	10.25	0.51	10.44	0.34	10.44	0.34	11.13	0.07	0.37	10.33	0.22	10.33	0.22	10.33	0.22		
0.17	0.05	0.19	0.05	0.18	0.05	0.15	0.04	0.17	0.14	0.04	0.15	0.04	0.16	0.04	0.16	0.04	0.16	0.02	0.16	0.05	0.16	0.05	0.16	0.05	0.16	0.05	
6.63	0.64	7.24	0.25	7.24	0.17	7.29	0.17	8.18	7.29	0.20	7.03	0.13	7.11	0.12	7.00	0.16	7.50	7.10	0.15	7.05	0.15	7.05	0.15	7.05	0.15	7.05	0.15
11.01	0.25	11.17	0.24	11.19	0.25	10.03	0.14	10.74	10.00	0.10	9.90	0.32	10.03	0.24	10.63	0.26	10.67	10.36	0.17	10.33	0.22	10.33	0.22	10.33	0.22	10.33	0.22
4.16	0.36	4.30	0.33	4.28	0.39	3.30	0.28	2.59	3.36	0.24	3.39	0.19	3.26	0.46	3.54	0.25	2.90	3.52	0.26	3.42	0.28	3.52	0.26	3.42	0.28	3.42	0.28
1.42	0.17	1.52	0.08	1.51	0.06	0.80	0.05	0.77																			

Case	YK16-01	YK16-01	YK16-01	YK16-01	YK16-01	YK16-08	YK16-08	YK16-08	YK16-08	YK16-08	YK16-08
Sample name	6K#1466R3-001	6K#1466R3-004	6K#1466R7-001	6K#1466R7-003	6K#1521R04	6K#1521R05	6K#1522R01	6K#1522R01	6K#1522R02	6K#1522R02	6K#1522R12
Sample type	Glass	Glass	Whole rock	Whole rock	LA-ICPMS						
μg/g											
Li	7.60	7.32				7.39	7.00	8.10		7.69	7.83
B	2.92	3.17				3.05	3.48	2.38		2.34	2.78
Sc	14.3	15.2	25.0	25.0		15.7	15.4	20.1	21.0	20.6	21.1
V	159	160	353	324		167	157	204	234	208	207
Cr	36.8	37.1	200	190		0.52	0.48	215	190	218	222
Co	29.7	29.9	61.0	57.0		32.8	31.2	46.2	49.0	46.8	47.3
Rb	47.5	47.6	26.0	32.0		34.1	33.4	25.8	28.0	26.9	26.6
Sr	976	991	577	307		1385	1361	848	827	924	943
Y	21.8	22.2	37.0	58.0		33.1	32.2	24.4	25.0	26.0	26.7
Zr	25.6	25.9	248	236		25.6	16.7	163	158	17.7	17.1
Nb	56.4	57.5	65.0	64.0		58.7	57.6	49.5	52.0	55.3	55.7
Cs	0.58	0.58				0.35	0.34	0.32		0.35	0.34
Ba	613	623	453	317		577	565	447	479	512	528
La	44.1	45.4	65.2	90.8		44.2	42.8	42.8	51.5	49.6	51.4
Ce	93.2	95.0	138	164		105	101	88.1	110	101	103
Pr	10.6	10.8	16.6	23.8		13.4	13.0	9.9	12.4	11.5	11.2
Nd	42.5	43.7	62.6	69.3		59.5	57.6	59.4	67.4	45.5	45.7
Sm	8.39	8.65	12.0	17.6		12.8	12.3	8.27	10.1	9.60	9.83
Eu	2.78	2.83	3.76	5.38		4.17	4.03	2.72	3.39	3.13	3.14
Gd	7.08	7.23	10.7	15.7		11.0	10.6	7.12	9.20	8.27	8.93
Tb	0.89	0.94	1.50	2.30		1.40	1.35	0.93	1.30	1.08	1.10
Dy	4.84	4.99	8.00	12.2		7.55	7.31	5.05	6.60	5.94	6.05
Er	0.79	0.81	1.30	2.10		1.24	1.19	0.82	1.10	0.97	1.00
Tm	0.23	0.25	0.44	0.69		0.34	0.34	0.22	0.31	0.26	0.29
Yb	1.43	1.48	2.60	4.10		2.12	2.02	1.40	1.70	1.64	1.69
Lu	0.19	0.19	0.36	0.60		0.28	0.26	0.18	0.24	0.22	0.23
Hf	5.33	5.54	5.80	6.20		6.42	6.12	3.14	3.90	3.76	4.01
Ta	3.04	2.81	4.80	5.30		3.34	2.93	2.01	2.80	2.34	2.37
Pb	3.55	3.39	-	6.00		2.82	2.59	3.06	-	3.68	3.59
Th	4.87	5.11	6.9	7.70		3.52	3.40	4.85	6.40	5.73	6.07
U	1.29	1.29	1.40	7.70		0.37	0.91	1.08	6.40	1.28	1.27

Table 3 continued  
\*: not detected  
#: Analyzed by ActLab

Case	YK18-08	YK18-08	YK19-05S								
Sample name	6K#1522R13	6K#1522R16	6K#1522R17	6K#1524R03	6K#1524R03	6K#1524R05	6K#1524R06	6K#1524R09	6K#1544R04	6K#1544R04	6K#1544R06
Sample type	Glass	Glass	Glass	Glass	Whole rock	Glass	Glass	Glass	Whole rock	Glass	Glass
μg/g											
8.06	8.53	8.42	5.54	5.52	6.00	6.19	6.21	6.20	6.20	6.16	6.16
2.83	2.77	2.94	1.60	1.88	1.89	1.80	2.28	2.28	2.38	2.14	2.14
21.5	19.7	20.6	22.5	22.3	22.7	23.7	22.0	22.0	22.8	23.6	23.6
217	213	209	189	188	200	201	203	203	197	191	191
231	203	203	334	350	317	269	292	292	305	295	295
44.3	47.2	46.8	42.3	40.0	42.7	42.1	41.8	44.9	47.0	43.4	42.0
28.0	30.3	28.7	14.2	14.0	14.5	17.4	17.4	17.0	17.0	16.4	16.4
930	1063	1086	565	487	568	622	643	579	519	595	604
27.0	27.9	29.6	22.8	20.0	22.4	22.5	23.7	22.9	21.0	24.0	25.1
173	184	194	122	120	122	134	140	123	122	128	132
55.7	64.2	65.7	24.0	23.0	24.1	25.1	25.9	27.0	25.0	27.3	27.4
0.36	0.41	0.40	0.19	-	0.20	0.22	0.21	0.25	-	0.25	0.23
514	584	590	255	219	254	292	301	286	259	297	297
49.3	58.1	60.9	26.8	26.1	26.6	28.6	29.8	27.8	28.0	28.8	29.5
101	120	122	56.6	62.8	56.5	58.8	60.4	59.8	66	60.9	60.0
11.5	13.3	13.8	6.86	7.37	6.79	7.10	7.42	7.20	7.60	7.34	7.41
46.6	53.3	53.7	29.3	30.0	29.3	30.3	31.7	30.4	31.5	31.3	31.8
9.71	10.8	11.4	6.65	7.00	6.64	8.82	7.21	8.78	7.10	7.10	7.27
3.21	3.58	3.67	2.24	2.41	2.23	2.28	2.38	2.34	2.42	2.39	2.44
8.57	9.42	9.92	6.29	6.80	6.26	6.53	6.82	6.45	6.90	6.75	6.90
1.12	1.20	1.27	0.85	1.00	0.85	0.87	0.93	0.89	1.00	0.91	0.96
6.10	6.38	6.81	4.89	5.30	4.83	4.88	5.10	4.91	5.40	5.17	5.33
1.00	1.02	1.10	0.98	0.90	0.92	0.84	0.97	0.84	0.90	0.89	0.91
2.45	2.47	2.23	2.12	2.30	2.13	2.10	2.22	2.10	2.30	2.27	2.32
0.28	0.28	0.30	0.26	0.28	0.26	0.26	0.26	0.26	0.29	0.28	0.27
1.70	1.67	1.75	1.57	1.70	1.57	1.52	1.60	1.58	1.70	1.66	1.71
0.22	0.21	0.22	0.21	0.23	0.21	0.20	0.22	0.21	0.22	0.23	0.23
3.95	4.08	4.36	2.95	3.10	2.95	3.20	3.39	2.95	3.00	3.12	3.18
2.40	2.63	2.77	1.96	1.30	1.16	1.16	1.23	1.21	1.40	1.23	1.24
3.71	4.38	4.26	1.67	-	1.78	1.82	1.85	1.84	1.98	1.86	1.82
5.69	6.88	7.29	2.47	2.80	2.47	2.78	2.89	2.72	3.00	2.85	2.85
1.31	1.57	1.58	0.62	2.80	0.63	0.66	0.66	0.71	3.00	0.68	0.65



461

463

Fig. 4. Relationships between the SiO<sub>2</sub> and alkali contents. (a) Total alkali vs. silica diagram using the platform of Le Bas et al. (1986). The dividing line of alkaline and sub-alkaline is from Irvine and Baragar (1971). The data are plotted as the total 100 wt%. The triangles and circles show the whole-rock and quenched-glass compositions, respectively. The compositions of the NW Pacific petit-spots are represented by gray triangles (Hirano and Machida, 2022). The data of the 6K#1203 and 1206 basalts are from Hirano et al. (2019), and those of the 6K#1466R7 basalts are from Mikuni et al. (2022). (b) K<sub>2</sub>O vs. Na<sub>2</sub>O diagram. The maximum K<sub>2</sub>O/Na<sub>2</sub>O value of kimberlite is from PetDB database (<https://search.earthchem.org/>). The data of OIB and MORB are compiled from Stracke et al. (2022) as “Expert datasets” in GEOROC database (<https://georoc.eu/georoc/new-start.asp>).

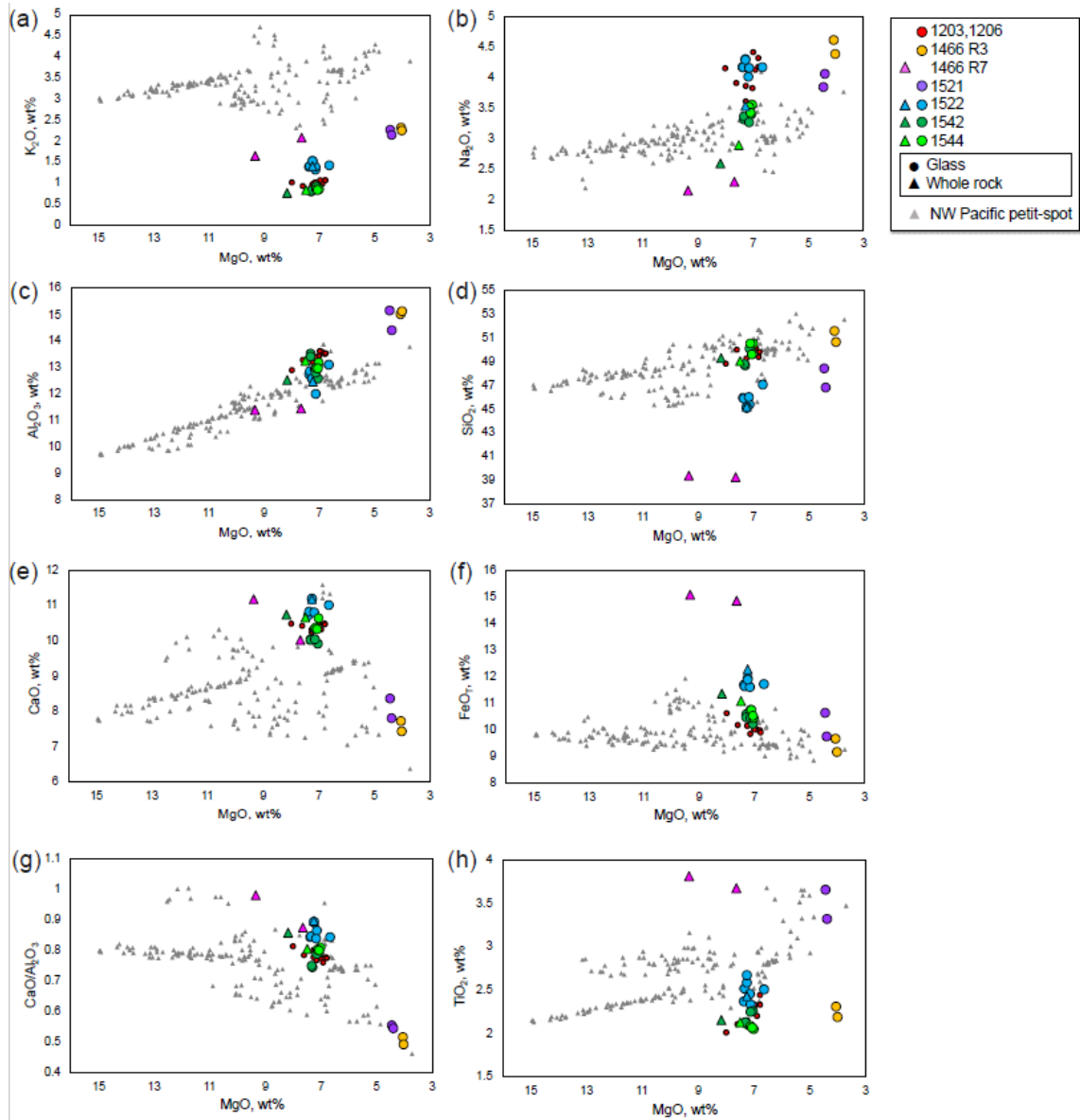
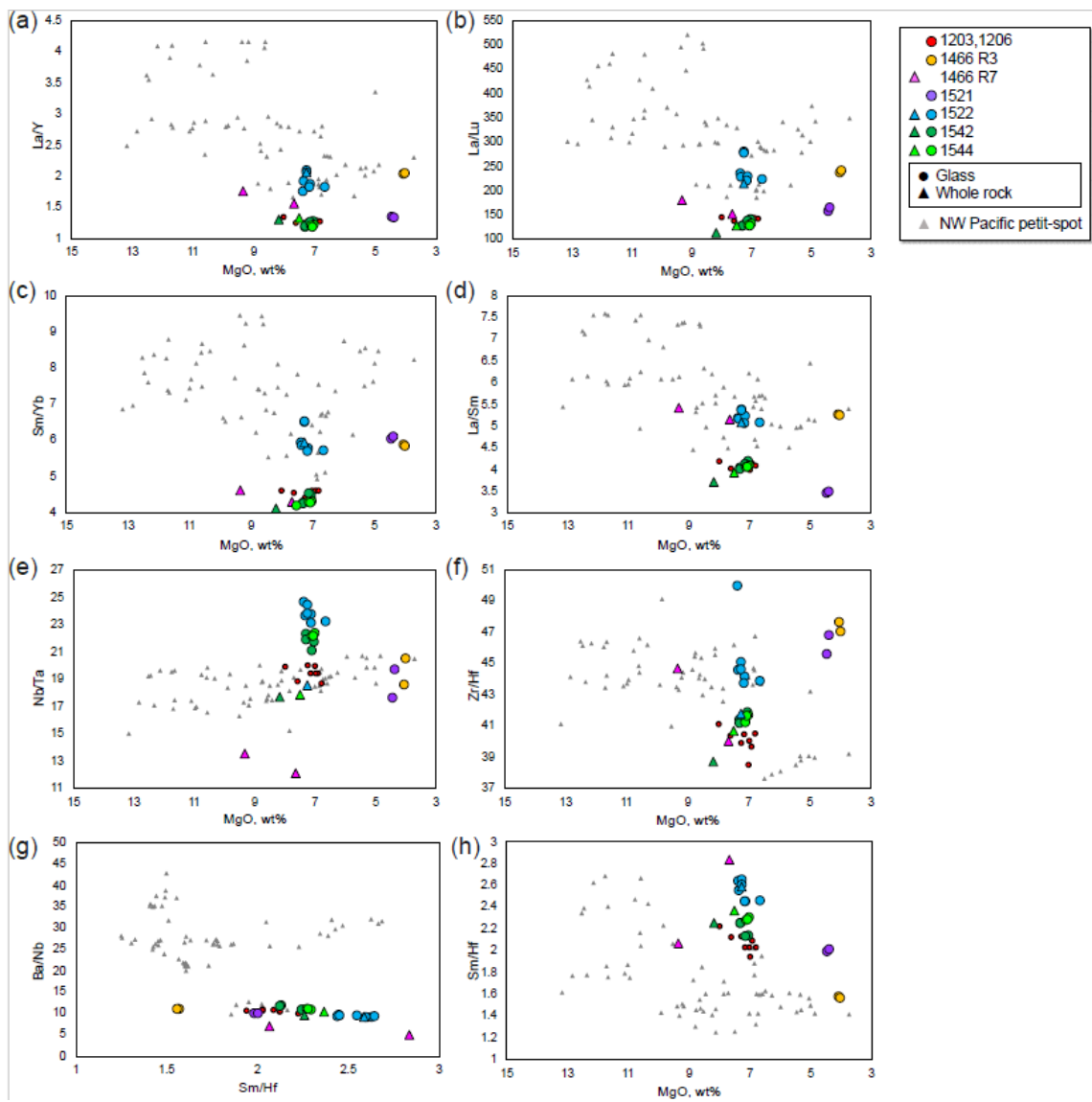


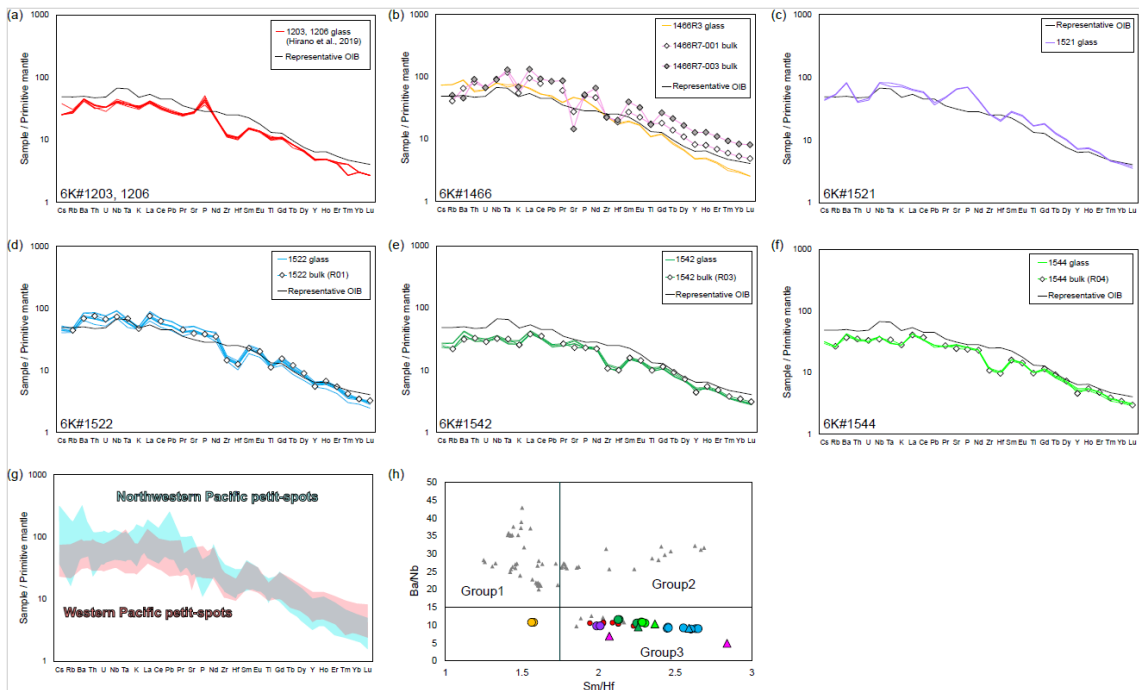
Fig. 5. Selected major-element oxides against MgO. The symbols and compiled data correspond to those in Fig. 3.



476

477 Fig. 6. Selected trace-element ratios against MgO. The symbols and compiled data correspond to those in Fig. 3.

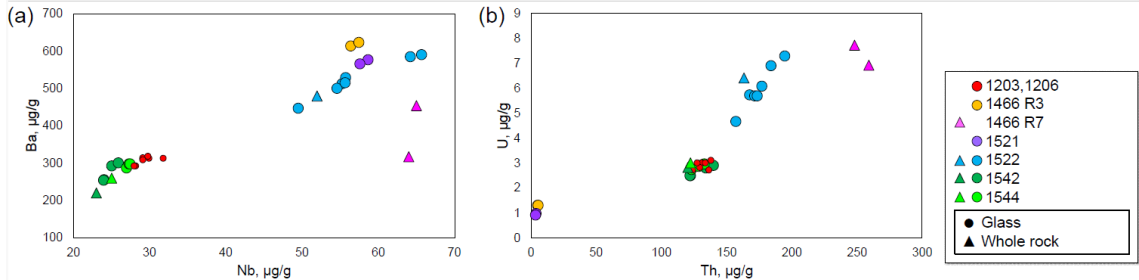
478



479

480 Fig. 7. Primitive mantle (PM, Sun and McDonough, 1989)-normalized trace-element patterns (a)–(g) and element  
 481 ratios (h). (g) The compositional range of the study samples and NW Pacific petit-spots (Hirano and  
 482 Machida, 2022). (h) The Ba/Nb and Sm/Hf ratios of the petit-spot basalts to discriminate the three groups  
 483 after Machida et al. (2015). The data of 6K#1203, 1206 basalts and 6K#1466R7 basalts are from Hirano  
 484 et al. (2019) and Mikuni et al. (2022), respectively. The symbols and compiled data in the (h) correspond  
 485 to those in Fig. 3.

486



487

488 Fig. 8. Alteration sensitive elements (Ba and U) vs. insensitive elements (Nb and Th). The symbols and compiled data  
 489 correspond to those in Fig. 3.

490

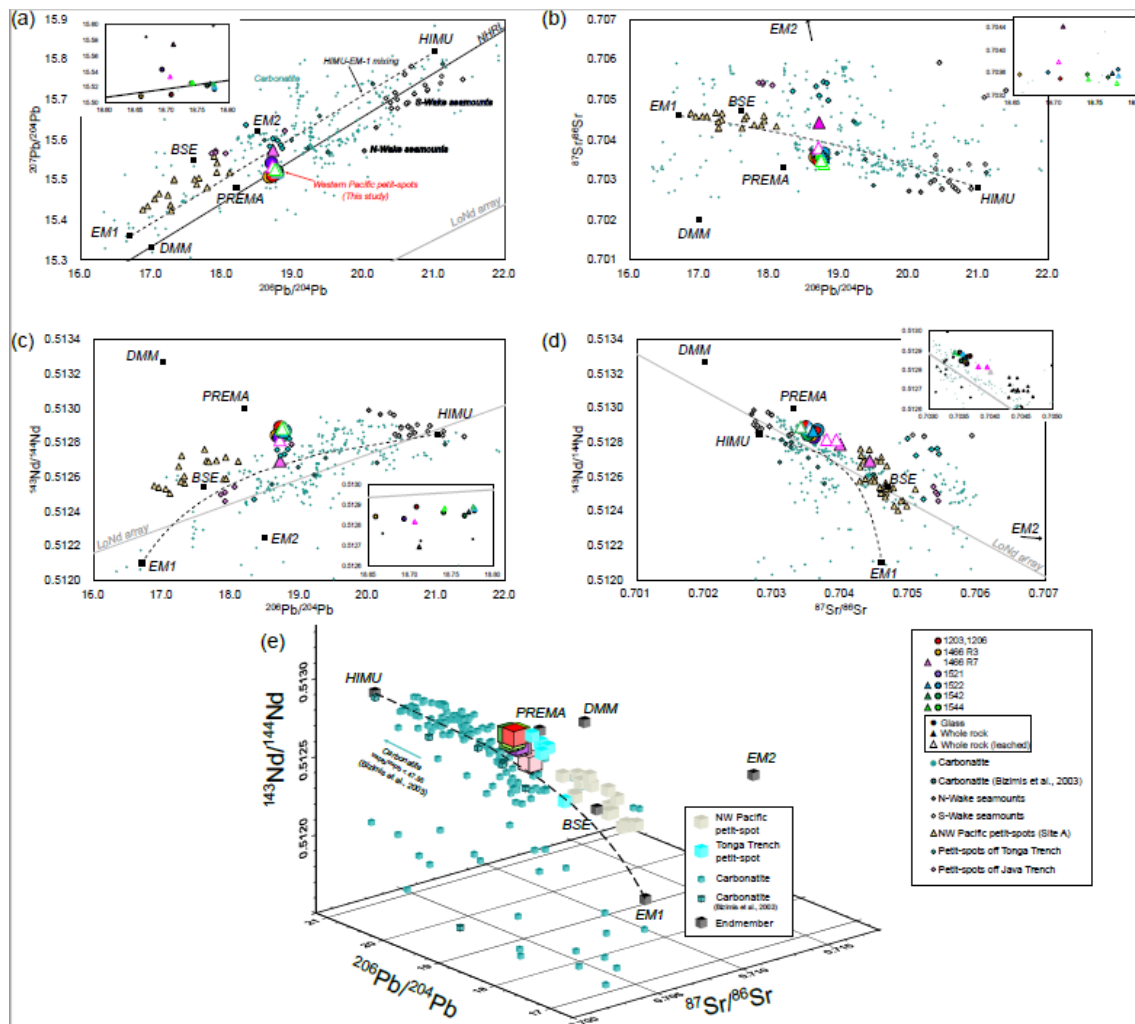
## 492 5.2 Sr–Nd–Pb isotopic composition

493

494 The Sr, Nd, and Pb isotopic compositions of the leached, unleached whole rock, and fresh glasses

495 in this study (presented in Table 4) were in practically identical ranges of  $^{87}\text{Sr}/^{86}\text{Sr}$  (0.703412–  
496 0.704424),  $^{143}\text{Nd}/^{144}\text{Nd}$  (0.512694–0.512890),  $^{206}\text{Pb}/^{204}\text{Pb}$  (18.6582–18.7778),  $^{207}\text{Pb}/^{204}\text{Pb}$  (15.5086–  
497 15.5749), and  $^{208}\text{Pb}/^{204}\text{Pb}$  (38.6506–38.8041) despite their different locations (Figs. 9a–d, Table 4).  
498 The isotopic compositions of the quenched glass and whole rock were identical, indicating that the  
499 characteristics of the melting source could be obtained through the geochemistry of the young and  
500 fresh volcanic quenched glass. The leached and unleached materials of the same sample also had  
501 similar isotopic ratios, except for the 1466R7-003 basalt, which had a relatively high LOI (6.29 wt%)  
502 (Figs. 9a–d). The Sr–Nd–Pb isotopic three-dimensional (3D) plot is shown in Fig. 9e.

503



504

505 Fig. 9. Sr–Nd–Pb isotopic variations of the petit-spot basalts. The mantle endmembers are derived from a study by  
506 Zindler and Hart (1986). The open triangles in (a)–(d) represent the acid-leached samples. Carbonatite  
507 data were compiled from GEOROC (<https://georoc.eu/georoc/new-start.asp>) with Bizimis et al. (2003).  
508 Carbonatite data with  $^{87}\text{Sr}/^{86}\text{Sr} > 0.706$  by GEOROC were eliminated. The northwestern (NW) Pacific  
509 petit-spots and petit-spots off the Tonga Trench are from Hirano and Machida (2022) and Reinhard et al.

(2019), respectively. The petit-spots off the Java trench are from Taneja et al. (2016) and Falloon et al. (2022). [The data of 1203 and 1206 basalts are from Hirano et al. \(2019\).](#) The data of the Wake seamounts are from studies by Konovalov and Martynov (1992), Koppers et al. (2003), Konter et al. (2008), Natland (1976), Smith et al. (1989), and Staudigel et al. (1991). The northern hemisphere reference line (NHRL) and Low Nd (LoNd) arrays are from studies by Hart (1984) and Hart et al. (1986), respectively. (e) The three-dimensional (3D) plot of the Sr–Nd–Pb isotopic compositions. The compilation and mantle endmembers correspond to (a)–(d). The color usages of the plots were the same as (a)–(d).

Table. 4  
Sr, Nd, and Pb isotopic compositions of western Pacific petit-spot basalts and measured standards.

Cruise	Sample name	Sample type	$^{87}\text{Sr}/^{86}\text{Sr}$	$^{143}\text{Nd}/^{144}\text{Nd}$	$^{206}\text{Pb}/^{204}\text{Pb}$	$^{207}\text{Pb}/^{204}\text{Pb}$	$^{208}\text{Pb}/^{204}\text{Pb}$	
YK16-01	6K#1466 R3-004	Glass	0.703568 (06)	0.512842 (05)	18.6582 (07)	15.5086 (06)	38.6506 (19)	
YK16-01	6K#1466 R7-001	Whole rock leached	0.703790 (05)	0.512817 (07)	18.7054 (20)	15.5337 (20)	38.8041 (50)	
YK16-01	6K#1466 R7-001	Whole rock unleached	0.703989 (05)	0.512790 (06)				
YK16-01	6K#1466 R7-003	Whole rock leached	0.703933 (11)	0.512815 (05)				
YK16-01	6K#1466 R7-003	Whole rock unleached	0.704424 (05)	0.512694 (05)	18.7107 (06)	15.5749 (06)	38.7618 (17)	
YK18-08	6K#1521 R04	Glass	0.703605 (05)	0.512832 (04)	18.6924 (06)	15.5428 (06)	38.7005 (19)	
YK18-08	6K#1522 R01	Whole rock leached	0.703544 (05)	0.512881 (06)	18.7778 (09)	15.5209 (08)	38.7991 (22)	
YK18-08	6K#1522 R01	Whole rock unleached	0.703590 (05)	0.512866 (06)	18.7705 (07)	15.5248 (07)	38.7905 (22)	
YK18-08	6K#1522 R01	Glass	0.703656 (06)	0.512872 (04)	18.7773 (08)	15.5178 (07)	38.7904 (21)	
YK19-05S	6K#1542 R03	Whole rock leached	0.703412 (07)	0.512890 (06)	18.7759 (10)	15.5244 (11)	38.7574 (36)	
YK19-05S	6K#1542 R05	Glass	0.703517 (06)	0.512847 (04)	18.7653 (08)	15.5224 (07)	38.7345 (19)	
YK19-05S	6K#1544 R04	Whole rock leached	0.703480 (04)	0.512883 (05)	18.7413 (14)	15.5262 (14)	38.745 (41)	
YK19-05S	6K#1544 R04	Glass	0.703568 (05)	0.512863 (04)	18.7400 (08)	15.5253 (09)	38.7347 (22)	
YK10-05	6K#1206 R04	Glass	0.703492 (05)	0.512890 (04)	18.7074 (06)	15.5109 (07)	38.6970 (19)	
YK10-05	6K#1206 R04 duplicate	Glass			18.7071 (07)	15.5119 (07)	38.6950 (18)	
Type of value	Standard for each isotope		$^{87}\text{Sr}/^{86}\text{Sr}$	$^{143}\text{Nd}/^{144}\text{Nd}$	$^{206}\text{Pb}/^{204}\text{Pb}$	$^{207}\text{Pb}/^{204}\text{Pb}$	$^{208}\text{Pb}/^{204}\text{Pb}$	
Analyzed value	JB-2			0.703721 (05)	0.513094 (04)	18.3326 (05)	15.5453 (06)	38.2240 (17)
Reference value	JB-2	Sr, Nd: Orihashi et al. (1998), Pb: Tanimizu and Ishikawa (2006)		0.703709 (29)	0.513085 (08)	18.3315 (25)	15.5460 (21)	38.2240 (55)
Analyzed value	JNd-1 (n=2)				0.512103 (05)			
Reference value	JNd-1	Wakaki et al. (2007)			0.512101 (11)			
Analyzed value	SRM987 (n=2)			0.710239 (05)				
Reference value	SRM987	Weis et al. (2006)		0.710254 (02)				
Analyzed value	SRM981					16.9303 (05)	15.4828 (06)	36.6710 (16)
Reference value	SRM981	Tanimizu and Ishikawa (2006)				16.9308 (10)	15.4839 (11)	36.6743 (30)

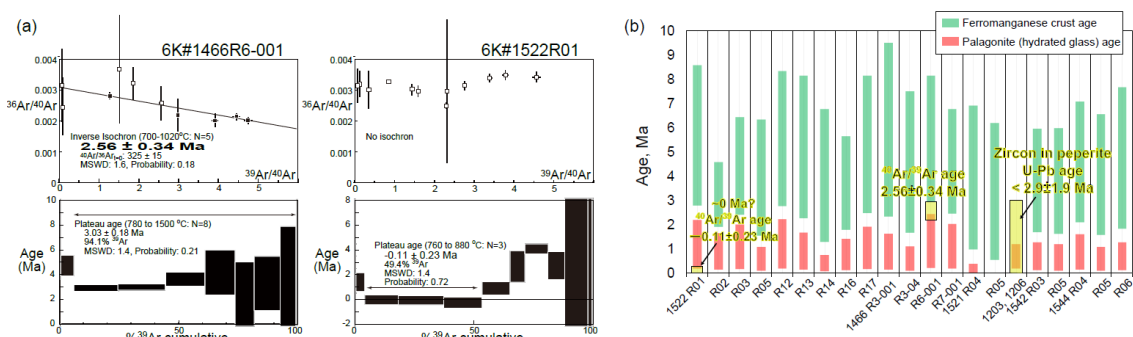
Errors shown in parentheses represent  $2\sigma$  and apply to the last two digits.

### 5.3 Age determination and estimation

The  $^{40}\text{Ar}/^{39}\text{Ar}$  ages were determined for two samples (1466R6-001 and 1522R01) (Fig. 10a, Table S4). The secondary material (e.g., alteration products) plausibly causes the recoil loss and redistribution of Ar during irradiation of samples, particularly fine-grained groundmass separates of submarine basalt (Koppers et al., 2000). This effect is negligible for  $^{40}\text{Ar}/^{39}\text{Ar}$  dating samples in this study because the total K/Ca ratios estimated using the irradiated  $^{39}\text{Ar}_\text{K}/^{37}\text{Ar}_\text{Ca}$  ratio (0.089 for 6K#1466R6, 0.080 for 6K#1522R01; Table S4) are mostly correspond to the bulk K/Ca ratios calculated using the major element compositions of Table 2 (0.088 for 6K#1466R71466R6-001, 0.076 for 6K#1522R01). This is supported by the rock descriptions recognized no secondary materials of

530 crystalline  $^{40}\text{Ar}/^{39}\text{Ar}$  specimens. Sample The 1466R6-001 sample had a plateau age of  $3.03 \pm 0.18$  Ma  
 531 in seven fractions comprising 94.1% released  $^{39}\text{Ar}$ . However, the plateau age was recognized as  
 532 apparently old, owing to excess  $^{40}\text{Ar}$ , as indicated by the initial  $^{40}\text{Ar}/^{36}\text{Ar}$  ratio of  $325 \pm 15$ , which  
 533 exceeded the atmospheric ratio (296.0; Nier, 1950) in the inverse isochron. The inverse isochron age  
 534 of  $2.56 \pm 0.34$  Ma showed the best age estimate for the 1466R6-001 basalt (Fig. 10a). The 1522R01  
 535 sample released almost no radiogenic daughter nuclide of  $^{40}\text{Ar}$  in the K–Ar age system (Fig. 10a).

536 The ranges of eruption age were estimated for all the samples using the average thickness ( $n =$   
 537 20) of ferromanganese crust and palagonite rind (hydrated quenched glass) with their  
 538 deposition/formation rates on the seafloor (ferromanganese crust, 1–10 mm/Myr; Hein et al., 1999;  
 539 palagonite, 0.03–0.3 mm/Myr; Moore et al., 1985) (Fig. 10b). Using this approach, the western Pacific  
 540 petit-spots were expected to have erupted later than ca. 9 Ma. The ranges of eruption age estimated  
 541 from palagonite rind did not overlap with those from ferromanganese crust showing older durations,  
 542 although they had general correlations (Fig. 10b). The  $^{40}\text{Ar}/^{39}\text{Ar}$  ages of two samples and the U-Pb  
 543 age of zircon in the 1203 and 1206 peperites (Hirano et al., 2019) were overlaid within these ranges.  
 544



545 Fig. 10. Geochronological data. (a) The  $^{40}\text{Ar}/^{39}\text{Ar}$  ages of the 6K#1466R6-001 and 6K#1522R01 basalts. The errors  
 546 show a 2-sigma confidence level. (b) Estimated relative ages using the thickness of ferromanganese crust  
 547 (green bands) and palagonite (hydrated quenched-glass rind; red bands) covered with petit-spot basalts.  
 548 These values were estimated using the average for each sample ( $n = 20$ ). The U-Pb age of zircon in the  
 549 6K#1203 and 1206 peperites are from Hirano et al. (2019).

551

## 552 6 Discussion

553

### 554 6.1 Eruptive setting of western Pacific petit-spots

555

556 Here In this study, two crystalline petit-spot basalts were subjected to  $^{40}\text{Ar}/^{39}\text{Ar}$  dating. A  
 557 previously reported investigated petit-spot knoll in this region (examined during the 6K#1203 and  
 558 #1206 dives) was dated aged at “younger than 3 Ma” was investigated using through the U–Pb dating

of eight zircons in peperites (Fig. 10b) (Hirano et al., 2019). The results ~~showed~~ ~~revealed~~ that the silica-undersaturated vesicular basalt of ~~6K#~~1466R6-001, ~~as a host of~~ ~~hosting~~ ultramafic xenoliths (Mikuni et al., 2022), exhibited a  $^{40}\text{Ar}/^{39}\text{Ar}$  age of  $2.56 \pm 0.34$  Ma (Fig. 10). ~~Opposely~~ ~~On the contrary~~, the fresh vesicular basalt of ~~6K#~~1522R01, which erupted at the foot of the 100-Ma Takuyo-Daigo seamount (Fig. 2) (Nozaki et al., 2016), did not exhibit radiogenic  $^{40}\text{Ar}$  ~~highlighting that this sample is quite indicating its young age (approximately 0 Ma)~~ (Fig. 10). The ranges of eruption ages were estimated using the average thickness of ferromanganese crust and palagonite rind (seawater-hydrated quenched glass) with their deposition/formation rates on the seafloor. The  $^{40}\text{Ar}/^{39}\text{Ar}$  and zircon U–Pb ages were within these ranges (Fig. 10). ~~Here, the~~ ~~petit-spot~~ volcanic field is surrounded by Cretaceous seamounts (Koppers et al., 2003) and irregular Paleogene volcanoes (Aftabuzzaman et al., 2021; Hirano et al., 2021). However, no zero-aged hotspots were observed in this region, and the P-wave tomographic image of the surface to the core–mantle boundary of the study area did not exhibit a plume-like low-velocity zone (Fig. 1c; Lu et al., 2019). Furthermore, the MORB-like to more depleted noble-gas isotopic compositions of the petit-spot knoll (~~investigated by~~ ~~6K#1203 and, #1206 dives~~) suggested its upper mantle origin (Yamamoto et al., 2018). Along with the outer-rise bulge in front of the Mariana Trench detected through a positive gravitational anomaly (Hirano et al., 2019), these data suggest that the western Pacific petit-spot volcanoes could have erupted at  $\sim$ 0–3 Ma owing to the flexure of the subducting Pacific Plate into the Mariana and Ogasawara Trenches.

The petit-spot basalts from the ~~6K#~~1542 and ~~#~~1544 dives could have originated from the same eruptive source based on their similar petrographic and geochemical features despite a distance of ~~approximately~~ ~~~~~6.8 km between both (Figs. 3d, 4, 5, 6, 7, 8, and 9). Contrarily, in terms of their petrography and geochemistry, the basalts from the ~~6K#~~1466 dive are ~~diseriminated~~ ~~distinguished~~ between the samples from the lava flows on the abyssal plain (~~1466~~R3-001 and ~~1466~~R3-004 ~~samples~~) and the samples from the knoll site (~~1466~~R6-001, ~~1466~~R7-001, and ~~1466~~R7-003 ~~samples~~). The ~~1466~~R3 basalts were collected at a lava outcrop 600 m south of the knoll, and the ~~1466~~R6 and ~~1466~~R7 samples were collected on the western slope of the knoll (Fig. 3a). The ~~6K#~~1466R3 series are glassy with a high  $\text{SiO}_2$  content (50.6–51.6 wt%), including minor plagioclase and ~~less~~ ~~fewer~~ vesicles (Figs. 3a and 4a). However, the ~~6K#~~1466R6 ~~and~~ ~~R~~7 series exhibited silica-undersaturated compositions ( $\text{SiO}_2 = 39.3$ –39.4 wt%) and high vesicularities (20–40 vol.%) (Figs. 3b and 4a). Combining these observations with the differences in  $\text{MgO}$  contents and trace element compositions, the ~~1466~~R3 and ~~1466~~R6–R7 basalts are implied to have different parental magmas (Figs. 6 and 7b). Generally, vesicular samples (~~6K#~~1203, 1206, ~~1466~~R7, 1522, 1542, and 1544 basalts) are relatively primary (i.e.,  $\text{MgO} > 6.63$  wt%), whereas nonvesicular samples (~~6K#~~1466R3 and 1521 basalts) are evolved (i.e.,  $\text{MgO} < 4.43$  wt%). This correlates with the compositions of olivine microphenocrysts in the low forsterite content ( $\text{Fo\#} = 100 \times \text{Mg}/[\text{Mg}+\text{Fe}^{2+}]_{\text{cation}}$ ) of olivine in evolved basalts and the high  $\text{Fo\#}$  of olivine in the relatively primary basalts (Figs. S1a–c).

595 The CI chondrite-normalized REE ratios of these samples are within those of OIBs, and the  
596 REE patterns exhibit HREE-depleted patterns (Fig. S3). However, among the western Pacific petit-  
597 spots, ~~the each volcano shows distinct~~ REE and trace element ratios ~~differ for each volcano~~ (i.e.,  
598 parental magmas) (Figs. 6 and S3). ~~Given Considering~~ the ~~absence~~ lack of correlation between MgO  
599 and the trace element ratios, ~~it is suggested that~~ each volcano could have originated from isolated  
600 sources (i.e., melt ponds) with ~~different varying~~ chemical compositions and degrees of melting (Fig.6).  
601 ~~Opposely~~On the contrary, the radiogenic Sr, Nd, and Pb isotopic ratios of the samples are nearly  
602 identical, ~~and indicating equivalent~~ the components in the source ~~are probably equivalent~~ (Fig. 9).

603 ~~Summarily~~In summary, (1) the western Pacific petit-spot volcanoes erupted at ~0–3 Ma owing  
604 to the plate flexure related to the subduction of the Pacific Plate into the Mariana Trench (Figs. 1 and  
605 2). (2) The ~~6K#~~1542 and 1544 samples originated during the same magmatic event (Fig. 3d). However,  
606 the basalts from the ~~6K#~~1466 dive ~~are subdivided~~were divided into two parental magmas (1466R3  
607 and 1466R6–R7 basalts) (Fig. 3a). (3) Each volcano originated from an isolated source and/or  
608 ascending processes ~~based on, as indicated by the~~ independent trace element ratios. ~~Despite this, t~~The  
609 geochemical components involved in the source, ~~however~~, were similar among the western Pacific  
610 petit-spot volcanoes ~~because of due to~~ the nearly identical Sr, Nd, and Pb isotopic compositions (Figs.  
611 6 and 9). ~~A~~The variation in ~~the~~ trace element compositions among the volcanoes is plausibly ~~due~~  
612 ~~attributed~~ to the degree of contribution of carbonatite flux and/or the recycled crustal component to  
613 the source, as discussed below.

## 615 6.2 Petit-spot magma composition and its evaluation

616  
617 Post-eruption ~~seawater~~ alteration ~~in seawater~~ ~~may~~ight have affected the chemical composition  
618 of oceanic basalts. Thus, various approaches, including petrographic observation, geochemical  
619 investigation, and acid leaching, have been employed to evaluate the primary features and the removal  
620 of this effect for isotopic analysis (Hanano et al., 2009; Melson et al., 1968; Miyashiro et al., 1971;  
621 Nobre Silva et al., 2009; Resing and Sansone, 1999; Staudigel and Hart, 1983; Zakharov et al., 2021).  
622 The study samples exhibit whole-rock LOI ~~of~~ <1.72 wt%, ~~excluding~~ ~~except for~~ two relatively altered  
623 samples, ~~6K#~~1466R7-001 (LOI = 2.68 wt%) and R7-003 (LOI = 6.29 wt%) basalts. Pristine quenched  
624 glasses are preserved in most of the samples, excluding three exceptional samples (~~the~~ ~~6K#~~1466R6-  
625 001, R7-001, and R7-003 basalts). Positive correlations ~~are observed~~exist between the alteration-  
626 insensitive (e.g., Nb, ~~and~~ Th) and -sensitive (e.g., Ba ~~and~~ U) incompatible elements. ~~This indicates,~~  
627 ~~indicating~~ that the effect of seawater alteration was not extensive, ~~excluding~~ ~~except for~~ the  
628 ~~6K#~~1466R7-001 and R7-003 basalts (Fig. 8). ~~Although each sample was derived~~Despite originating  
629 from different volcanic edifices, the positive correlation of all the study samples is ~~due~~attributed to  
630 the chemical similarity of ~~the~~ source compositions for certain elements (i.e., the Ba/Nb and U/Th ratios

631 are nearly constant among the samples), as well as the Sr, Nd, and Pb isotopic compositions (Fig. 9).  
632 These ~~observations showed~~findings demonstrate that most of the petit-spot basalts were largely  
633 unaffected by seawater alteration, with a few exceptions (i.e., 1466R7-001 and R7-003 basalts).

634 The ~~variable~~ MgO (4–9 wt%), Ni (<263 ppm), and Cr (<350 ppm) contents in the samples are  
635 lower than the expected values of primary mantle-derived melt (MgO >10 wt%, Ni >400 ppm, Cr  
636 >1000 ppm; Frey et al., 1978). Similarly, the Mg# ( $100 \times \text{Mg}/[\text{Fe}^{2+} + \text{Mg}]_{\text{molar}}$ ) values ~~are differentiated~~  
637 ~~in the~~ range ~~from~~of 41 ~~to~~ to 57 (Table 2) against the primary basaltic melt, which is equilibrated with  
638 the upper mantle (Mg# = 66–75; Irving and Green, 1976). No phenocrysts were observed (only  
639 microphenocryst), despite such differentiated compositions as well as most of the NW Pacific petit-  
640 spot basalts. This suggests that the western Pacific petit-spots experienced crystal fractionation in the  
641 lithosphere as well as the case ~~of~~in the NW Pacific petit-spot (Machida et al., 2017; Valentine and  
642 Hirano, 2010; Hirano, 2011; Yamamoto et al., 2014). ~~Consequently~~Therefore, ~~the~~ calculation  
643 ~~of~~calculating the primary composition of the petit-spot basalts using the mineral modal composition  
644 on the thin section ~~could~~was not ~~be~~performed~~possible~~. However, the major element trends of ~~the~~  
645 ~~major elements~~ of the samples ~~imply~~indicate the crystal fractionation of the same phases. ~~The~~  
646 ~~the~~ Negative trends of the  $\text{Al}_2\text{O}_3$  content and the positive trends ~~of~~in the CaO and  $\text{CaO}/\text{Al}_2\text{O}_3$  content  
647 with ~~a decrease in~~decreasing MgO indicate the occurrence of olivine, spinel, and clinopyroxene  
648 fractionation (Figs. 5c, e, and g). The absence of visible correlations of ~~the~~  $\text{K}_2\text{O}$ ,  $\text{Na}_2\text{O}$ ,  $\text{SiO}_2$ , and  $\text{TiO}_2$   
649 contents against MgO suggests ~~that the~~insignificant fractionation of plagioclase and ~~the~~ Fe–Ti oxides  
650 ~~was~~was ~~insignificant~~. The Fe–Ti oxides as minor phases in the groundmasses and plagioclases were only  
651 observed in the most differentiated 1466R3-001 and R3-004 basalts (Figs. 3, 5a, b, d, and h). However,  
652 these major elemental trends should be interpreted as apparent ~~trends~~ because each petit-spot volcano  
653 originated from an isolated parental magma with ~~a~~ different chemical composition or degree of partial  
654 melting, as discussed above.

655 The melting source of alkali basalts can be determined more effectively by examining their trace  
656 element composition ~~of alkali basalts can be used to determine the melting source~~ rather than major  
657 elements (Hofmann, 2003; Machida et al., 2014, 2015). Trace element composition of magma,  
658 however, could be modified by crustal and/or mantle assimilation and fractionation of ~~certain~~specific  
659 minerals. The relatively primitive basalts (6K#1203, 1206, 1466R6, R7, 1522, 1542, and 1544  
660 samples) included~~contained~~ xenocrystic olivines and partly ultramafic xenoliths, suggesting~~indicating~~  
661 a rapid magma ascent (Hirano et al., 2019; Mikuni et al., 2022; Fig. S4). However, since the stagnation  
662 of ascending petit-spot magma could ~~occur~~lead to the formation of~~erate~~ fertile peridotite and  
663 pyroxene-rich veins ~~from~~in the middle to lower depths of the lithosphere (Mikuni et al., 2022; Pilet  
664 et al., 2016), the chemical composition of the petit-spot magma could be modified ~~because of~~through  
665 assimilation with ~~the~~ ambient lithospheric peridotite. According to Hirano and Machida (2022),  
666 ascending silica-undersaturated melt would predominantly~~mainly~~ consume orthopyroxene ( $\pm$  spinel)

and ~~become result in~~ a more silicic composition with Zr and Hf depletion. This is ~~because of due to~~ the relatively higher Zr–Hf partition of orthopyroxene than ~~those of compared to~~ other trace elements (Pilet et al., 2008; Shaw, 1999; Tamura et al., 2019). The orthopyroxenes of fertile pyroxenites and lherzolite xenoliths metasomatized by petit-spot melts exhibit Zr and Hf enrichment (Mikuni et al., 2022; Fig. S5). If this silica-enrichment (i.e., melt–rock interaction) was significant, a positive correlation between  $\text{SiO}_2$  and Sm/Hf is expected as a mantle assimilation trend. However, the samples ~~exhibit exhibited~~ a negative correlation, similar to those of the NW Pacific petit-spots (Hirano and Machida, 2022) (Fig. S2). Considering the relationship between the Sm and Hf partition coefficients of clinopyroxene (i.e.,  $D^{Hf} < D^{Sm}$ ; McKenzie and O’Nions, 1991; Kelemen et al., 2003), we suggest that the negative correlation between the Sm/Hf and  $\text{SiO}_2$  ~~of in~~ the petit-spot basalts probably reflects the crystal fractionation of clinopyroxene rather than mantle assimilation. The Ba/Nb ratios of the samples are nearly constant and do not correlate with the MgO and  $\text{SiO}_2$  contents (Figs. 6g and S2g). The lack of correlation between ~~the~~ other trace element ratios, excluding Sm/Hf and Ba/Nb (i.e., La/Y, La/Lu, Sm/Yb, La/Sm, Nb/Ta, Zr/Hf), and the MgO concentration ~~imply suggests~~ that crystal fractionation may not have been involved ~~with in~~ those of the incipient melt (Fig. 6). However, ~~it is difficult to~~ independently ~~follow tracking~~ the evolution of the trace element composition for each volcano ~~since is challenging, given that~~ each volcano originated from isolated sources. Thus, considering the observations above, the fresh and zero-aged ~~6K#~~1522 basalts (~~having~~ the highest Sm/Hf ratios and lowest  $\text{SiO}_2$  contents among the fresh samples and higher MgO contents) were selected for further analysis with geochemical modeling. ~~Considering Given~~ that the ~~6K#~~1522 samples had MgO in the range of 6.63–7.36 wt%, olivine was expected ~~to be~~ the dominant phase of crystal fractionation (Asimow and Langmuir, 2003; Helz and Thornber, 1987; Herzberg, 2006). ~~When By applying~~ the olivine maximum fractionation model (Takahashi et al., 1986; Tatsumi et al., 1983) ~~was applied~~ to test two samples, ~~it was noted that 7–9% olivine addition was required to achieve the olivine composition corresponding to “Mantle olivine array” in the NiO and Fo# spaces (Figs. S6a, b). The~~ calculated primary trace element contents did not ~~significantly considerably~~ differ from those of the analytical compositions (Table S5 and Fig. S6). Thus, the ~~6K#~~1522 basalts were assumed to be the most primary petit-spot basalt samples and were used to evaluate the geochemical modeling results.

### 6.3 Melting source of western Pacific petit-spots

The depletions ~~observed in~~ specific elements (e.g., Ta, Zr, Hf, and Ti) ~~in the~~ petit-spot basalts potentially demonstrate the involvement of carbonatitic materials in conjunction with a large amount of  $\text{CO}_2$  and lower Mg isotopic ratio than that of the normal mantle (Bizimis et al., 2003; Dasgupta et al., 2009; Hirano and Machida, 2022; Hoernle et al., 2002; Liu et al., 2020; Okumura and Hirano, 2013). Other oceanic lavas originating from the asthenosphere (e.g., Hawaiian rejuvenated

703 lavas and North Arch volcanoes) exhibited characteristic trace element signatures (i.e., Zr and Hf  
704 depletion) similar to those of petit-spot lavas. This implies that their melting sources were involved  
705 with carbonatitic materials with or without plume-derived components (Fig. S7; Borisova and Tilhac,  
706 2021; Clague and Frey, 1982; Clague et al., 1990; Dixon et al., 2008; Yang et al., 2003). ~~In~~  
707 ~~addition~~Additionally, the involvement of recycled crustal components was inferred from the  
708 geochemical features of the petit-spot basalts, and the upper mantle was revealed to be heterogeneous  
709 (Liu et al., 2020; Machida et al., 2009, 2015). Such a scenario of the source ~~on~~for petit-spot magma  
710 ~~aligns~~is consistent with the previously suggested petrogenesis of alkaline rocks explained by the  
711 addition of CO<sub>2</sub>-rich components and/or recycled crustal materials with or without sediment to the  
712 mantle (e.g., Dasgupta et al. 2007; Hofmann, 1997). Conversely, the melting of an amphibole-rich  
713 metasomatic vein explains the major and trace element composition of alkali basalts (Pilet et al., 2008;  
714 Pilet, 2015). However, the experimentally produced melts exhibit Pb depletion and a positive Nb-Ti  
715 anomaly in the PM-normalized trace element patterns (Fig. S8), which is inconsistent with the petit-  
716 spot basalts (Fig. 7). ~~In addition~~Moreover, Juriček and Keppler (2023) demonstrated that amphibole  
717 dehydration is not the cause for the oceanic LAB ~~by~~through high-pressure experiments ~~under~~on the  
718 realistic condition~~s~~. The fertile pyroxenitic xenoliths and pyroxene xenocrysts ~~occurring~~ in the 1466R6  
719 and R7 basalts, ~~which~~ originating from the metasomatic vein related to prior petit-spot magmatism,  
720 had neither amphiboles nor other hydrous minerals (Mikuni et al., 2022).

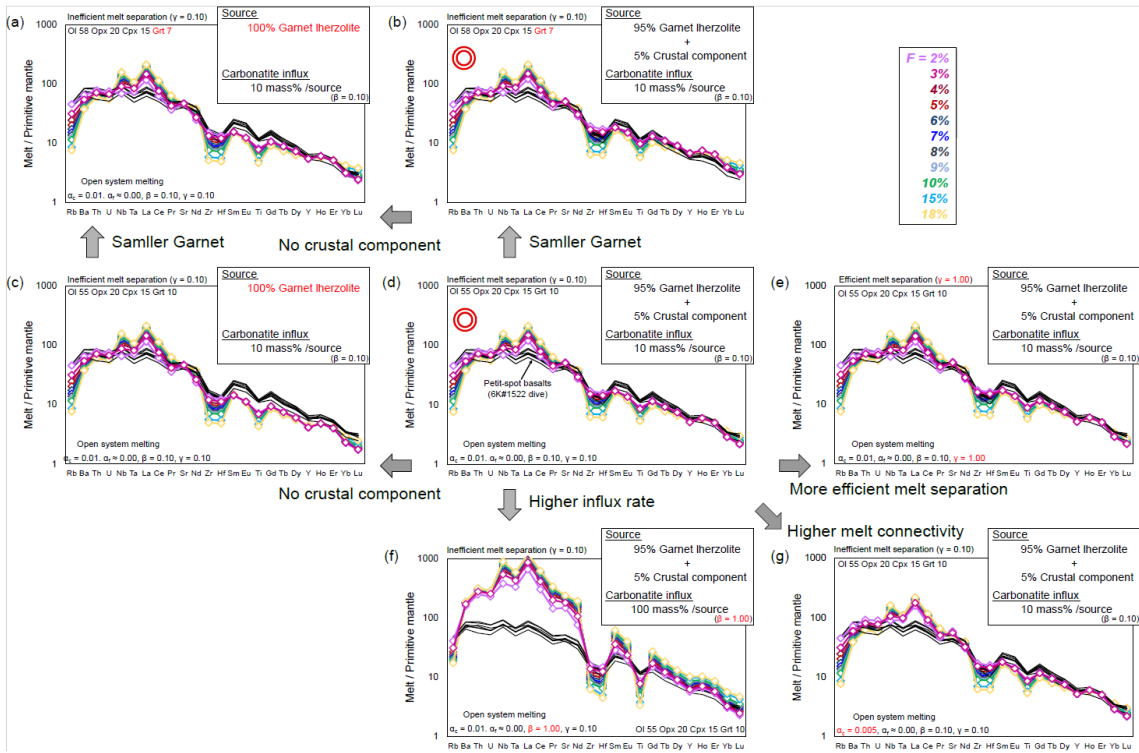
721 To ~~discuss~~explore the involvement of carbonatitic and crustal components in petit-spot melts,  
722 a partial melting model of the heterogeneous mantle is ~~provided~~presented. The involvement of  
723 carbonatitic fluids and recycled materials in the genesis of petit-spot melts has been suggested, and  
724 the open-system model with carbonatite influx from the outer system was employed using “OSM-4”  
725 ~~ef~~by Ozawa (2001), ~~and~~ by referring the parameters ~~by~~of Borisova and Tilhac (2021). This model is  
726 based on the mass conservation equations of one-dimensional steady-state melting. In this ~~present~~  
727 study, the model ~~uses~~ assumes the critical melt fraction ( $\alpha_c$ ; mass fraction of melt when melt separation  
728 begins = melt connectivity threshold) at 0.005 or 0.01. The system ~~is~~opens to fluxing at a  
729 constant melt-separation rate ( $\gamma$ ) when the system reaches the  $\alpha_c$ . The final trapped melt fraction ( $\alpha_f$ ;  
730 mass fraction of melt trapped in the residue) was fixed at ~0 (it was calculated as 10<sup>-6</sup> owing to mass  
731 balance). We calculated the trace element composition of partial melts at various degrees~~s~~ of melting  
732 ( $F$ ) ~~as well as~~ a few rates of influx ( $\beta$ ) and melt separation ( $\gamma$ ). We assumed a primitive mantle (PM)  
733 source as ~~a~~the lherzolite with or without a normal (N)-MORB source as the recycled oceanic crust  
734 (Sun and McDonough, 1989), such as pyroxenite and eclogite. The recycled crust (N-MORB  
735 component) was mixed in the source as compositional heterogeneity calculated as “0.05N-MORB +  
736 0.95PM” for ~~the~~ trace element concentration~~s~~, ~~and~~ the considered The mineral phases and their  
737 proportions considered were derived only from garnet lherzolite (i.e., olivine, orthopyroxene,  
738 clinopyroxene, and garnet). The mineral mode of garnet lherzolite (olivine 55%, orthopyroxene 20%,

739 clinopyroxene 15%, and garnet 10%) and the melting reaction mode (olivine 8%, orthopyroxene –19%,  
740 clinopyroxene 81%, and garnet 30%) are based on studies by Johnson et al. (1990) and Walter (1998),  
741 respectively. The proportion of olivine and garnet was also changed to ~~evaluate-assess~~ the effect of ~~the~~  
742 garnet modal ratio ~~onto~~ the produced melt composition. In this situation, the clinopyroxene is  
743 consumed at ~~an F~~ (degree of partial melting) of ~ 19%; ~~hence therefore~~, the system was calculated up  
744 to 18% partial melting. The carbonatite melt ~~used, as an influx~~, in this model ~~as a influx~~ is “average  
745 carbonatite” from a study by Bizimis et al. (2003). The partition coefficient of trace elements is  
746 generally based on a study by McKenzie and O’Nions (1991, 1995),~~excluding Ti for clinopyroxene~~  
747 and garnet (Kelemen et al., 2003). The variables of  $\beta$  (influx rate) and  $\gamma$  (melt-separation rate) were  
748 changed during the modeling within the mass balance ( $\gamma \leq \beta + 1$ ). The modeled melts were outputted  
749 as “total melt,” considering the instantaneous and accumulated melts. For the carbonatite composition,  
750 the value of “average carbonatite” ~~of from~~ Bizimis et al. (2003) is applied because the chemical  
751 composition of carbonatite is largely diverse, and this value is recommended for geochemical  
752 modeling (Bizimis et al., 2003). The parameters are ~~listed detained~~ in Table S6. ~~Consequently As a~~  
753 ~~result~~, partial melting of garnet lherzolite with ~~a~~ 10% carbonatite influx to a given mass of source (i.e.,  
754 garnet lherzolite) can ~~roughly explain provide a rough explanation of~~ the trace element pattern of petit-  
755 spot basalts (Figs. 11a–e),~~and~~ ~~The most plausible for petit-spot magma generation involves~~ the  
756 presence of ~~a~~ 5% crustal component in the source ~~is the most plausible model of petit spot magma~~  
757 ~~generation~~ (Figs. 11b and d). In addition, ~~having~~ slightly less garnet in the lherzolite source than the  
758 modal ratio of Johnson et al. (1990) ~~fits offers a better fit for the~~ petit-spot ~~characteristics better~~ (Fig.  
759 11b). In both ~~cases scenarios~~, ~~the presence of incorporating~~ a crustal component in the source ~~yields~~  
760 ~~produces~~ more plausible ~~results outcomes~~ (Figs. 11a–d). The higher carbonatite influx ( $\beta = 1.0$ ) could  
761 not explain the trace element composition of the petit-spot basalts (Fig. 11f). ~~The A~~ melt connectivity  
762 threshold ( $\alpha_c$ ) of 0.01 is ~~considered~~ plausible, ~~as because~~ higher connectivity of melt (i.e., lower  $\alpha_c$   
763 value) leads to enrichment of LILEs and LREEs (Fig. 11g). The results also ~~showed indicate~~ that the  
764 melt-separation ratio ~~is has no~~ ~~insignificant impact onto~~ the trace element composition of the  
765 calculated melts (Figs. 11d and e). Thereafter, we concluded that the partial melting of ~5% crustal  
766 component-bearing garnet lherzolite with ~10% carbonatite flux to a given mass of the source  
767 plausibly explains the melting source of petit-spot volcanoes (Figs. 11b and d). Assuming that the trace  
768 element composition of ~~6K#~~1203, 1206, 1542, and 1544 basalts are also primitive, they ~~may could~~ be  
769 explained by ~~a the~~ partial melting of garnet lherzolite with 5% crustal component and lower carbonatite  
770 influx rate ( $\beta = 0.03$ ) (Fig. S9). Actually, the ~~6K#~~1203, 1206, 1542, and 1544 basalts exhibited ~~the~~  
771 similar MgO contents and Mg# to those of ~~the~~ ~~6K#~~1522 basalts (Fig. 4 and Table 2). These results  
772 provide quantitative evidence ~~on the petrogenesis of petit-spots~~regarding petit-spots' petrogenesis, i.e.,  
773 the contribution of carbonatite melt and recycled oceanic crust.

774 Although the melting source ~~contained included~~ small proportions of carbonatite melt and

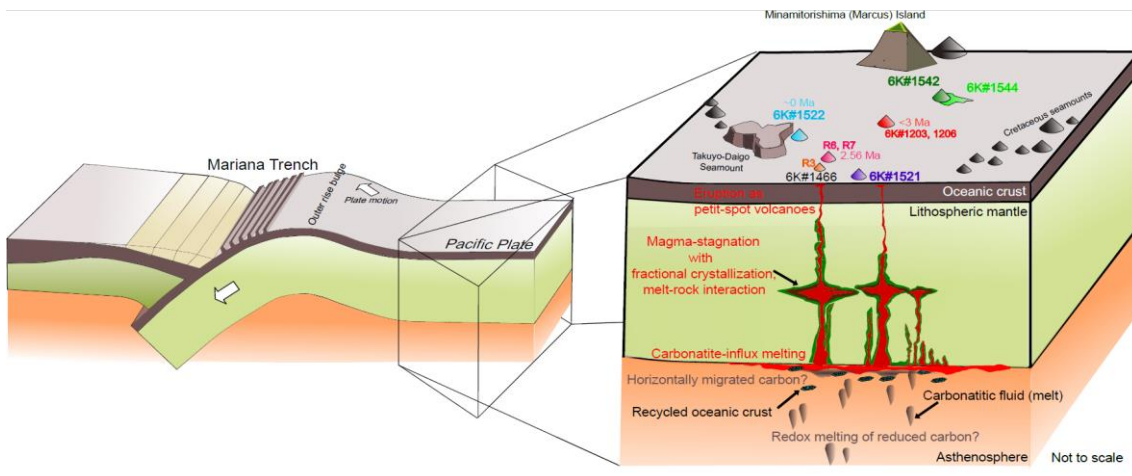
775 crustal components, these components could have contributed to the isotopic composition because  
776 following to their abundant incompatible elements, as opposed to rather than the ambient mantle. The  
777 determination of the Sr, Nd, and Pb isotopic compositions revealed indicated that they had  
778 geochemically identical prevalent mantle (PREMA)-like sources (Fig. 9). Contrary to those of NW  
779 Pacific petit-spots, which exhibit EM-1 isotopic composition (Machida et al., 2009; Liu et al., 2020),  
780 the samples herein did They do not align with belong to any mantle isotopic endmembers (i.e., depleted  
781 MORB mantle (DMM); EM-1 and, EM-2; and HIMU; Fig. 9) contrary to those of NW Pacific petit-  
782 spots toward the EM-1 isotopic composition (Machida et al., 2009; Liu et al., 2020). In the Pb isotopic  
783 space, the present samples do did not correlate with those of the neighboring HIMU-like Cretaceous  
784 seamounts (Fig. 9a) (N-Wake, S-Wake seamounts; Konter et al., 2008; Koppers et al., 2003; Natland,  
785 1976; Smith et al., 1989; Staudigel et al., 1991). For the melting source of the NW Pacific petit-spot  
786 basalts, the contributions involvement of the eclogite/pyroxenite endmember as recycled oceanic crust  
787 and the carbonated endmember were was suggested. This suggestion was based on the major and trace  
788 elements and the Mg, Sr, Nd, and Pb isotopic compositions with the Mg diffusion modeling (Liu et  
789 al., 2020). The higher FeO/MnO ratios of observed in the present melts (65.9–78.0), compared to with  
790 those of partial melts originating from peridotite (50–60), are attributed to the presence of recycled  
791 pyroxenite (Herzberg, 2011). This could have contributed, potentially contributing to the crustal  
792 components in the melting source. However, the western Pacific petit-spots in this study identically  
793 exhibited uniformly displayed a PREMA-like isotopic signature without extreme endmember  
794 contributions as described previously above (Fig. 9). Such isotopic compositions with the world's  
795 petit-spots can be possibly explained by the diverse mixing proportion of HIMU and EM-1  
796 components (Fig. 9e). The isotopic compositions of the NW Pacific petit-spots (off the Japan Trench),  
797 Samoan petit-spots (off the Tonga Trench), petit-spot dikes in Christmas Island (off the Java trench),  
798 and western Pacific petit-spots (off the Mariana Trench in this study) are roughly along the HIMU–  
799 EM-1 mixing line (Fig. 9e). Furthermore, the isotopic compositions of global carbonatites can be  
800 generally be explained by the mixing of HIMU and EM-1 (Bell and Tilton, 2002; Hoernle et al., 2002;  
801 Hulett et al., 2016). The contributions of the carbonated material/carbonatite and crustal components  
802 to the melting source were suggested in terms relation to the origin of HIMU and EM-1 (Collerson  
803 et al., 2010; Hanyu et al., 2011; Wang et al., 2018; Weiss et al., 2016; Workman et al., 2004; Zindler  
804 and Hart, 1986). However, the determination of EM-1 and HIMU components a could not be  
805 determined to be carbonated components and recycled crust, respectively, is challenging due to  
806 the various perspectives views on each tectonic setting for the mantle endmember. The variability of  
807 global carbonatite isotopic compositions also makes it difficult to determine poses challenges in  
808 determining their representative isotope ratios (Fig. 9). Although such issues make Despite these  
809 challenges hindering a quantitative isotopic mixing model challenging, the HIMU-EM-1-like trend  
810 observed in of the global petit-spot volcanoes suggests may reflect the involvement of carbonatitic and

recycled crustal materials. ~~Conclusively~~In conclusion, the mass balance models ~~on the applied to~~ trace elements and the isotopic variations in the petit-spot volcanoes confirmed the contribution of carbonatite melt and the recycled oceanic crust to the melting source of the western Pacific petit-spots (Fig. 12). Experimental studies have revealed the ~~various diverse~~ petrogenesis scenarios of carbonatite and carbonatitic alkali-rich magma under high pressures (Dasgupta et al., 2006; Ghosh et al., 2009). The geochemistry of petit-spot basalts including Mg isotopes suggested that the conceivable origin of carbonatite related to the petit-spot melt is subducted “carbonated” pelite, pyroxenite/eclogite, or peridotite stored as diamond or metal carbide in the reduced lower portion of the upper mantle (Liu et al., 2020; Rohrbach et al., 2007). ~~For instance, subducted carbonated pelite, for example, would melt under high pressure (>8 GPa) through the oxidation at the redox boundary where the iron-wüstite (IW) buffer changes to the quartz–fayalite–magnetite (QFM) buffer (i.e., redox melting; Grassi and Schmidt, 2011). Chen et al. (2022) demonstrated that the alkali-rich carbonatite melt could occur under at a pressure higher than exceeding 6 GPa, particularly exhibiting K-rich and Na-rich carbonatites under 6–12 and >12 GPa, respectively. This pressure-dependent alkalinity of the produced resulting carbonatite melts could potentially account for might explain the differences variation between potassic NW Pacific petit-spot lavas and present sodic petit-spot lavas (Fig. 4b). On the other hand, an experimental study pointed out highlighted the existence presence of a carbonate-rich layer in the LAB owing to the horizontally spread carbonate from around the wedge mantle rather than upwelling from the deep mantle (Hammouda et al., 2020). Several high pressure–temperature experiments and modeling revealed that the chemical composition of intraplate magmas originating from the upper mantle depends on their original depth. Specifically, the carbonatitic melt can be generated beneath thick cratonic lithosphere (~250–200 km), kimberlitic melt would could be produced at >120 km in depth, and alkali basalt would could occur at 100–60 km in depth by the partial melting of “original” CO<sub>2</sub> and H<sub>2</sub>O-bearing mantle (Massuyeu et al., 2021). These This depth-dependent compositional variation in composition, i.e. that is, K-rich kimberlite to alkali basalt, may also explain provide an explanation for the geochemical gap between K-rich NW Pacific petit-spots and K-poor western Pacific petit-spots (Fig. 4b). Although the multiple origins of carbonatite are merely suggested and remain unclear, carbon-rich components play a key role in the partial melting of mantle at the LAB (Sifré et al., 2014), that is, constituting the source of petit-spot magma.~~



840

841 Fig. 11. Geochemical modeling for the primitive mantle (PM)-normalized trace-element pattern. The calculated  
 842 hypothetical melts are a production of carbonatite influx melting of garnet Iherzolite with or without 5%  
 843 crustal component. Detailed information of the parameters is described in Section 6-3 and Table S6.  $F$  is  
 844 the degree of melting (%). The trace-element composition of the western Pacific petit-spot basalts from  
 845 the 6K#1522 dive is shown as black lines for comparison. The PM composition of Iherzolite and the N-  
 846 MORB composition of recycled crust were based on a study by Sun and McDonough (1989). The influx  
 847 carbonatite is the “average carbonatite” of a study by Bizimis et al. (2003). The parameters used in the  
 848 open-system melting models were as follows:  $a_c$  is a critical melt fraction,  $a_f$  is a final trapped melt  
 849 fraction,  $\beta$  is a melt influx rate, and  $\gamma$  is a melt-separation rate. Model results are compared by varying  
 850 each parameter, i.e., garnet modal ratio and presence of crustal material (a-d), melt-separation rate (d and  
 851 e), carbonatite influx rate (d and f), and critical melt fraction (d and g). Each figure is expressed based on  
 852 the difference from the condition in (d).  
 853



854

855 Fig. 12. Schematic illustration of the magmatic processes of the western Pacific petit-spot volcanoes.

856 Carbonatitic melt and recycled oceanic crust potentially induce partial melting of asthenospheric mantle  
 857 beneath the western Pacific region. Carbonatitic melt might have originated from a carbon-rich  
 858 component horizontally migrated from a subduction zone (Hammouda et al., 2020), or a redox melting  
 859 of reduced carbon in the deep mantle (Chen et al., 2022; Grassi and Schmidt, 2011; Rohrbach et al., 2007).  
 860 Petit-spot magma stagnated in the lithosphere with fractional crystallization and melt-rock interaction  
 861 (Mikuni et al., 2022), and they have erupted at ~0–3 Ma.

862

## 863 7 Conclusion

864

865 The occurrence of petit-spot volcanism supports partial melting at the LAB, providing  
 866 erucialcarryingsignificant implications for the naturecharacteristics of this geophysical discontinuity.  
 867 MultipleNumerousinstancesof petit-spot magmatismsoccurred on the western Pacific Plate occurred  
 868 at ~0–3 Ma, originating from similar PREMA-like melting sources based on  $^{40}\text{Ar}/^{39}\text{Ar}$  dating and the  
 869 Sr, Nd, and Pb isotopic compositions. The mass balance-based open-system modeling for trace  
 870 elements revealed that the western Pacific petit-spot magma was generated by the partial melting of a  
 871 small amount (5%) of oceanic crust-bearing garnet lherzolite with 3%–10% carbonatite influx to a  
 872 given mass of the source. The Sr, Nd, and Pb-isotopic compositions of Sr, Nd, and Pb of thethis study  
 873 samples, in conjunction with those of the NW Pacific petit-spots, petit-spots off the Tonga and Java  
 874 Trenches, could be explained by mixing the EM-1-like and HIMU-like components, which  
 875 contributinge to the subducted carbonated/crustal materials. The tectonic-induced magmatism, such  
 876 aslike a petit-spot, may followhavethesameasimilar melting mechanism.

877

## 878 Authorship contributions

879

880 K. Mikuni and N. Hirano conceived the project and performed all experiments. S. Machida and  
 881 Y. Kato contributed the Sr, Nd, and Pb isotopic analysis using TIMS and MC-ICP-MS. H. Sumino

882 contributed the  $^{40}\text{Ar}/^{39}\text{Ar}$  dating. N. Akizawa, A. Tamura, and T. Morishita helped and performed  
883 EPMA and LA-ICP-MS analyses. S. Machida and N. Hirano conducted the research cruises to gain  
884 the rock samples. All authors interpreted the data and wrote the manuscript with comments and  
885 improvements.

886

### 887 Competing Interest

888

889 The authors declare that they have no conflict of interest.

890

### 891 Data availability

892

893 The data newly analyzed in this study and results of geochemical modeling are included in  
894 digital format in the online data repository of this paper (Tables 1, 2, 3 and 4, and Supplementary  
895 Tables S1 to S6) and the EarthChem online database (DOI will be obtained when it is accepted).

896

### 897 Acknowledgement

898

899 We would like to thank the captains, crews, and shipboard scientific parties of the R/V *Yokosuka*  
900 and the operating team of the submersible *Shinkai* 6500 for their great work during the YK16-01,  
901 YK18-08, and YK19-05S cruises. The Kyoto University Research Reactor Institute is greatly  
902 acknowledged in their assistance of undertaking the radiometric dating. We would like to express our  
903 great appreciation to Prof. T. Tsujimori (ORCID: 0000-0001-9202-7312) for his effort in management  
904 of the laboratory at Tohoku University. We also thank R. Fukushima (ORCID: 0000-0003-2683-6757)  
905 for improving the wording in the manuscript. We are really grateful Y. Matamura, Y. Shimbo, and Y.  
906 Jindo for their help and discussion on scientific matters. The authors would like to thank Enago  
907 ([www.enago.jp](http://www.enago.jp)) for the English language review. This research was supported by the Cooperative  
908 Program (No. 106, 202) of Atmosphere and Ocean Research Institute, The University of Tokyo. The  
909 Japan Society for the Promotion of Science (Grant Numbers 17K05715, 18H03733, 20K04098) also  
910 supported this research.

911

### 912 References

913

914 Aftabuzzaman, M.R., Yomogoda, K., Suzuki, S., Takayanagi, H., Ishigaki, A., Machida, S., Asahara,  
915 Y., Yamamoto, K., Hirano, N., Sano, S.-I., Chiyonobu, S., Bassi, D. and Iryu, Y.: Multi-  
916 approach characterization of shallow-water carbonates off Minamitorishima and their  
917 depositional settings/history, Island Arc, 30, e12400, <https://doi.org/10.1111/iar.12400>, 2021.

918 Akizawa, N., Ozawa, K., Tamura, A., Michibayashi, K. and Arai, S.: Three-dimensional evolution of  
919 melting, heat and melt transfer in ascending mantle beneath a fast-spreading ridge segment

920 constrained by trace elements in clinopyroxene from concordant dunites and host  
921 harzburgites of the Oman ophiolite, *J. Petrol.*, 57, 777–814,  
922 <https://doi.org/10.1093/petrology/egw020>, 2016.

923 Akizawa, N., Ohara, Y., Okino, K., Ishizuka, O., Yamashita, H., Machida, S., Sanfilippo, A., Basch,  
924 V., Snow, J.E., Sen, A., Hirauchi, K.-I., Michibayashi, K., Harigane, Y., Fujii, M., Asanuma,  
925 H. and Hirata, T.: Geochemical characteristics of back-arc basin lower crust and upper  
926 mantle at final spreading stage of Shikoku Basin: an example of Mado Megamullion, *Prog.  
927 Earth Planet. Sci.*, 8, 65, <https://doi.org/10.1186/s40645-021-00454-3>, 2021.

928 Akizawa, N., Hirano, N., Matsuzaki, K.M., Machida, S., Tamura, C., Kaneko, J., Iwano, H.,  
929 Danhara, T. and Hirata, T.: A direct evidence for disturbance of whole sediment layer in the  
930 subducting Pacific plate by petit-spot magma–water/sediment interaction, *Mar. Geol.*, 444,  
931 106712, <https://doi.org/10.1016/j.margeo.2021.106712>, 2022.

932 Asimow, P. D. and Langmuir, C. H.: The importance of water to oceanic mantle melting regimes,  
933 *Nature*, 421, 815–820, <https://doi.org/10.1038/nature01429>, 2003.

934 Audhkhasi, P. and Singh, S.C.: Discovery of distinct lithosphere–asthenosphere boundary and the  
935 Gutenberg discontinuity in the Atlantic Ocean, *Sci. Adv.*, 8, eabn5404,  
936 <https://doi.org/10.1126/sciadv.abn5404>, 2022.

937 Axen G.J., van Wijk, J.W. and Currie, C.A.: Basal continental mantle lithosphere displaced by flat-  
938 slab subduction, *Nat. Geosci.*, 11, 961–964, <https://doi.org/10.1038/s41561-018-0263-9>,  
939 2018.

940 Azami, K., Machida, S., Hirano, N., Nakamura, K., Yasukawa, K., Kogiso, T., Nakanishi, M. and  
941 Kato, Y.: Hydrothermal ferromanganese oxides around a petit-spot volcano on old and cold  
942 oceanic crust, *Commun. Earth Environ.*, 4, 191, <https://doi.org/10.1038/s43247-023-00832-3>, 2023.

944 Bell, K. and Tilton, G. R.: Probing the mantle: the story from carbonatites, *Eos*, 83, 273–277,  
945 <https://doi.org/10.1029/2002EO000190>, 2002.

946 Bellas, A., Zhong, S. and Watts, A.B.: Reconciling lithospheric rheology between laboratory  
947 experiments, field observations and different tectonic settings, *Geophys. J. Int.*, 228, 857–  
948 875, <https://doi.org/10.1093/gji/ggab382>, 2022.

949 Bianco, T.A., Ito, G., Becker, J.M. and Garcia, M.O.: Secondary Hawaiian volcanism formed by  
950 flexural arch decompression, *Geochem. Geophys. Geosyst.* 6, Q08009,  
951 <https://doi.org/10.1029/2005GC000945>, 2005.

952 Bizimis, M., Salters, V.J.M. and Dawson, J.B.: The brevity of carbonatite sources in the mantle:  
953 evidence from Hf isotopes, *Contrib. to Mineral. Petrol.*, 145, 281–300,  
954 <https://doi.org/10.1007/s00410-003-0452-3>, 2003.

955 Bizimis, M., Salters, V.J.M., Garcia, M.O. and Norman, M.D.: The composition and distribution of

956 the rejuvenated component across the Hawaiian plume: Hf-Nd-Sr-Pb isotope systematics of  
957 Kaula lavas and pyroxenite xenoliths, *Geochem. Geophys. Geosyst.* 14, 4458–4478,  
958 <https://doi.org/10.1002/ggge.20250>, 2013.

959 Borsova, A.Y. and Tilhac, R.: Derivation of Hawaiian rejuvenated magmas from deep carbonated  
960 mantle sources: A review of experimental and natural constraints, *Earth. Sci. Rev.*, 222,  
961 103819, <https://doi.org/10.1016/j.earscirev.2021.103819>, 2021.

962 Buchs, D.M., Pilet, S., Cosca, M., Flores, K.E., Bandini, A.N. and Baumgartner, P.O.: Low-volume  
963 intraplate volcanism in the Early/Middle Jurassic Pacific basin documented by accreted  
964 sequences in Costa Rica, *Geochem. Geophys. Geosyst.*, 14, 1552–1568,  
965 <https://doi.org/10.1002/ggge.20084>, 2013.

966 Chantel, J., Manthilake, G., Andrault, D., Novella, D., yu, T. and Wang, Y.: Experimental evidence  
967 supports mantle partial melting in the asthenosphere, *Sci. Adv.*, 2, e1600246,  
968 <https://doi.org/10.1126/sciadv.1600246>, 2016.

969 Chen, X., Wang, M., Inoue, T., Liu, Q., Zhang, L. and Bader, T.: Melting of carbonated pelite at 5.5–  
970 15.5 GPa: implications for the origin of alkali-rich carbonatites and the deep water and  
971 carbon cycles, *Contrib. to Mineral. Petrol.*, 177, 2, <https://doi.org/10.1007/s00410-021-01867-5>, 2022.

973 Clague, D.A. and Frey, F.A.: Petrology and Trace element Geochemistry of the Honolulu Volcanics,  
974 Oahu: Implications for the Oceanic Mantle below Hawaii, *J. Petrol.*, 23, 447–504,  
975 <https://doi.org/10.1093/petrology/23.3.447>, 1982.

976 Clague, D.A., Holcomb, R.T., Sinton, J.M., Detrick, R.S. and Torresan, M.E.: Pliocene and  
977 Pleistocene alkali flood basalts on the seafloor north of the Hawaiian island, *Earth Planet.  
978 Sci. Lett.*, 98, 175–191, [https://doi.org/10.1016/0012-821X\(90\)90058-6](https://doi.org/10.1016/0012-821X(90)90058-6), 1990.

979 Clague, D.A., Moore, J.G.: The proximal part of the giant submarine Wailau landslide, Molokai,  
980 Hawaii, *J. Volcanol. Geotherm. Res.*, 113, 259–287, [https://doi.org/10.1016/S0377-0273\(01\)00261-X](https://doi.org/10.1016/S0377-<br/>981 0273(01)00261-X), 2002.

982 Collerson, K.D., Williams, Q., Ewart, A.E. and Murphy, D.T.: Origin of HIMU and EM-1 domains  
983 sampled by ocean island basalts, kimberlites and carbonatites: The role of CO<sub>2</sub>-fluxed lower  
984 mantle melting in thermochemical upwellings, *Phys. Earth Planet. Inter.*, 181, 112–131,  
985 <https://doi.org/10.1016/j.pepi.2010.05.008>, 2010.

986 Conrad, C.P., Bianco, T.A., Smith, E.I. and Wessel, P.: Patterns of intraplate volcanism controlled by  
987 asthenospheric shear, *Nat. Geosci.*, 4, 317–321, <https://doi.org/10.1038/ngeo1111>, 2011.

988 Cousens, B.L. and Clague, D.A.: Shield to Rejuvenated Stage Volcanism on Kauai and Niihau,  
989 Hawaiian Islands, *J. Petrol.*, 56, 1547–1584, <https://doi.org/10.1093/petrology/egv045>,  
990 2015.

991 Dasgupta, R. and Hirschmann, M.M.: Melting in the Earth's deep upper mantle caused by carbon

992 dioxide, *Nature*, 440, 659–662, <https://doi.org/10.1038/nature04612>, 2006.

993 Dasgupta, R., Hirschmann, M.M. and Stalker, K.: Immiscible Transition from Carbonate-rich to  
994 Silicate-rich Melts in the 3 GPa Melting Interval of Eclogite + CO<sub>2</sub> and Genesis of Silica-  
995 undersaturated Ocean Island Lavas, *J. Petrol.*, 47, 647–671,  
996 <https://doi.org/10.1093/petrology/egi088>, 2006.

997 Dasgupta, R., Hirschmann, M.M. and Smith, N.D.: Partial Melting Experiments of Peridotite + CO<sub>2</sub>  
998 at 3 GPa and Genesis of Alkalic Ocean Island Basalts, *J. Petrol.*, 48, 2093–2124,  
999 <https://doi.org/10.1093/petrology/egm053>, 2007.

1000 Dasgupta, R., Hirschmann, M.M., McDonough, W.F., Spiegelman, M. and Withers, A.: Trace  
1001 element partitioning between garnet lherzolite and carbonatite at 6.6 and 8.6 GPa with  
1002 applications to the geochemistry of the mantle and of mantle-derived melts, *Chem. Geol.*,  
1003 262, 57–77, <https://doi.org/10.1016/j.chemgeo.2009.02.004>, 2009.

1004 Dasgupta, R., Mallik, A., Tsuno, K., Withers, A.C., Hirth, G. and Hirschmann, M.M.: Carbon-  
1005 dioxide-rich silicate melt in the Earth's upper mantle, *Nature*, 493, 211–215,  
1006 <https://doi.org/10.1038/nature11731>, 2013.

1007 Debayle, E., Bodin, T., Durand, S. and Ricard, Y.: Seismic evidence for partial melt below tectonic  
1008 plates, *Nature*, 586, 555–559, <https://doi.org/10.1038/s41586-020-2809-4>, 2020.

1009 Dixon, J., Clague, D.A., Cousens, B., Monsalve, M.L. and Uhl, J.: Carbonatite and silicate melt  
1010 metasomatism of the mantle surrounding the Hawaiian plume: evidence from volatiles, trace  
1011 elements, and radiogenic isotopes in rejuvenated-stage lavas from Niihau, Hawaii,  
1012 *Geochem. Geophys. Geosyst.*, 9, Q09005, <https://doi.org/10.1029/2008GC002076>, 2008.

1013 Ebisawa, N., Sumino, H., Okazaki, R., Takigami, Y., Hirano, N., Nagao, K. and Kaneoka, I.:  
1014 Construction of I-Xe and <sup>40</sup>Ar–<sup>39</sup>Ar dating system using a modified VG3600 noble gas mass  
1015 spectrometer and the first I-Xe data obtained in Japan, *J. Mass Spectrom. Soc. Jpn.*, 52,  
1016 219–229, <https://doi.org/10.5702/massspec.52.219>, 2004.

1017 Falloon, T. J. and Green, D. H.: The solidus of carbonated, fertile peridotite. *Earth Planet. Sci. Lett.*  
1018 94, 364–370, [https://doi.org/10.1016/0012-821X\(89\)90153-2](https://doi.org/10.1016/0012-821X(89)90153-2), 1989.

1019 Falloon, T. J. and Green, D. H.: Solidus of carbonated fertile peridotite under fluid-saturated  
1020 conditions. *Geology*, 18, 195–199, [https://doi.org/10.1130/0091-7613\(1990\)018<0195:SOCPFU>2.3.CO;2](https://doi.org/10.1130/0091-7613(1990)018<0195:SOCPFU>2.3.CO;2), 1990.

1022 Falloon, T.J. Hoernle, K., Schaefer, B.F., Bindeman, I.N., Hart, S.R., Garbe-Schonberg, D. and  
1023 Duncan, R.A.: Petrogenesis of Lava from Christmas Island, Northeast Indian Ocean:  
1024 Implications for the Nature of Recycled Components in Non-Plume Intraplate Settings,  
1025 *Geosci.*, 12, 118, <https://doi.org/10.3390/geosciences12030118>, 2022.

1026 Frey, F.A., Green, D.H. and Roy, S.D.: Integrated Models of Basalt Petrogenesis: A Study of Quartz  
1027 Tholeiites to Olivine Melilitites from South Eastern Australia Utilizing Geochemical and



1064 HIMU reservoir: A possible mantle plume source in the lower mantle, *Geochem. Geophys.*  
1065 *Geosyst.*, 12, Q0AC09, <https://doi.org/10.1029/2010GC003252>, 2011.

1066 Hanyu, T., Shimizu, K., Ushikubo, T., Kimura, J.-I., Chang, Q., Hamada, M., Ito, M., Iwamori, H.  
1067 and Ishikawa, T.: Tiny droplets of ocean island basalts unveil Earth's deep chlorine cycle,  
1068 *Nat. Commun.*, 10, 60, <https://doi.org/10.1038/s41467-018-07955-8>, 2019.

1069 Hart, S.R.: A large-scale isotope anomaly in the Southern Hemisphere mantle, *Nature*, 309, 753–757,  
1070 <https://doi.org/10.1038/309753a0>, 1984.

1071 Hart, S.R., Gerlach, D.C. and White, W.M.: A Possible new Sr-Nd-Pb mantle array and consequences  
1072 for mantle mixing, *Geochim. Cosmochim. Acta.*, 50, 1551–1557,  
1073 [https://doi.org/10.1016/0016-7037\(86\)90329-7](https://doi.org/10.1016/0016-7037(86)90329-7), 1986.

1074 Hein, J.R., Koschinsky, A., Bau, M., Manheim, F.T., Kang, J.K. and Roberts, L.: Cobalt-rich  
1075 ferromanganese crusts in the Pacific, *Handbook of Marine Mineral Deposits* (Cronan DS,  
1076 ed.), 239–279, CRC Press, Boca Raton, Florida, 1999.

1077 Helz, R.T. and Thronber, C.R.: Geochemistry if Kilauea Iki lava lake, Hawaii, *Bull. Volcanol.*, 49,  
1078 651–658, <https://doi.org/10.1007/BF01080357>, 1987.

1079 Herath, P., Stern, T.A., Savage, M.K., Bassett, D. and Henrys, S.: Wide-angle seismic reflections  
1080 reveal a lithosphere-asthenosphere boundary zone in the subducting Pacific Plate, New  
1081 Zealand, *Sci. Adv.*, 8, eabn5697, <https://doi.org/10.1126/sciadv.abn5697>, 2022.

1082 Herzberg, C.: Petrology and thermal structure of the Hawaiian plume from Mauna Kea volcano,  
1083 *Nature*, 444, 605–609. <https://doi.org/10.1038/nature05254>, 2006.

1084 Herzberg, C.: Identification of Source Lithology in the Hawaiian and Canary Islands: Implications  
1085 for Origins, *J. Petrol.*, 52, 113–146, <https://doi.org/10.1093/petrology/egq075>, 2011.

1086 Hirano, N., Takahashi, E., Yamamoto, J., Abe, N., Ingle, S.P., Kaneoka, I., Hirata, T., Kimura, J.-I.,  
1087 Ishii, T., Ogawa, Y., Machida, S. and Suyehiro, K.: Volcanism in response to plate flexure.  
1088 *Science*, 313, 1426–1428. <https://doi.org/10.1126/science.1128235>, 2006.

1089 Hirano, N.: Petit-spot volcanism: a new type of volcanic zone discovered near a trench, *Geochem. J.*,  
1090 45, 157–167, <https://doi.org/10.2343/geochemj.1.0111>, 2011.

1091 Hirano, N., Machida, S., Abe, N., Morishita, T., Tamura, A. and Arai, S.: Petit-spot lava fields off the  
1092 central Chile trench induced by plate flexure, *Geochem. J.*, 47, 249–257,  
1093 <https://doi.org/10.2343/geochemj.2.0227>, 2013.

1094 Hirano, N., Nakanishi, M., Abe, N. and Machida, S.: Submarine lava fields in French Polynesia,  
1095 *Mar. Geol.*, 373, 39–48, <http://dx.doi.org/10.1016/j.margeo.2016.01.002>, 2016.

1096 Hirano, N., Machida, S., Sumino, H., Shimizu, K., Tamura, A., Morishita, T., Iwano, H., Sakata, S.,  
1097 Ishii, T., Arai, S., Yoneda, S., Danhara, T. and Hirata, T.: Petit-spot volcanoes on the oldest  
1098 portion of the Pacific Plate, *Deep Sea Res. Part I*, 154, 103142,  
1099 <https://doi.org/10.1016/j.dsr.2019.103142>, 2019.

1100 Hirano, N., Sumino, H., Morishita, T., Machida, S., Kawano, T., Yasukawa, K., Hirata, T., Kato, Y.  
1101 and Ishii, T.: A Paleogene magmatic overprint on Cretaceous seamounts of the western  
1102 Pacific, Island Arc, 30, e12386, <https://doi.org/10.1111/iar.12386>, 2021.

1103 Hirano, N. and Machida, S.: The mantle structure below petit-spot volcanoes, Commun. Earth  
1104 Environ., 3, 110, <https://doi.org/10.1038/s43247-022-00438-1>, 2022.

1105 Hirth, G. and Kohlstedt, D.L.: Water in the oceanic upper mantle: implications for rheology, melt  
1106 extraction and the evolution of the lithosphere. Earth Planet. Sci. Lett., 144, 93–108,  
1107 [https://doi.org/10.1016/0012-821X\(96\)00154-9](https://doi.org/10.1016/0012-821X(96)00154-9), 1996.

1108 Hoernle, K., Tilton, G., Le Bas, M.J., Duggen, S. and Garbe-Schönberg, D.: Geochemistry of  
1109 oceanic carbonatites compared with continental carbonatites: mantle recycling of oceanic  
1110 crustal carbonate, Contrib. to Mineral. Petrol., 142, 520–542,  
1111 <https://doi.org/10.1007/s004100100308>, 2002.

1112 Hofmann, A.W.: Mantle geochemistry: the message from oceanic volcanism, Nature, 385, 219–229,  
1113 <https://doi.org/10.1038/385219a0>, 1997.

1114 Hofmann, A.W.: Sampling mantle heterogeneity through oceanic basalts: isotopes and trace  
1115 elements. In: Carson, R. W. (Ed.), Treatise on Geochemistry, 2, The Mantle and Core,  
1116 Elsevier, 61–101, <https://doi.org/10.1016/B0-08-043751-6/02123-X>, 2003.

1117 Hosseini, K., Matthews, K.J., Sigloch, K., Shephard, G.E., Domeier, M. and Tsekhmistrenko, M.:  
1118 SubMachine: Web-Based tools for exploring seismic tomography and other models of  
1119 Earth's deep interior, Geochem. Geophys. Geosyst., 19, 1464–1483,  
1120 <https://doi.org/10.1029/2018GC007431>, 2018.

1121 Hua, J., Fisher, K. M., Becker, T.W., Gazel, E. and Hirth, G.: Asthenospheric low-velocity zone  
1122 consistent with globally prevalent partial melting, Nat. Geosci., 16, 175–181,  
1123 <https://doi.org/10.1038/s41561-022-01116-9>, 2023.

1124 Hulett, S.R., Simonetti, A., Rasbury, E.T. and Hemming, N.G.: Recycling of subducted crustal  
1125 components into carbonatite melts revealed by boron isotopes, Nat. Geosci., 9, 904–908,  
1126 <https://doi.org/10.1038/ngeo2831>, 2016.

1127 Irvine, T. N. and Baragar, W. R. A.: A Guide to the Chemical Classification of the Common Volcanic  
1128 Rocks, Can. J. Earth Sci., 8, 523–548, <https://doi.org/10.1139/e71-055>, 1971.

1129 Irving, A.J and Green, D.H.: Geochemistry and petrogenesis of the newer basalts of Victoria and  
1130 South Australia, J. Geol. Sci. Australia., 23, 45–66,  
1131 <https://doi.org/10.1080/00167617608728920>, 1976.

1132 Iwata, N.: Geochronological study of the Deccan volcanism by the  $^{40}\text{Ar}$ – $^{39}\text{Ar}$  method, Doctor  
1133 Thesis, University of Tokyo, pp. 168, 1998.

1134 Jochum, K.P. and Nohl, U.: Reference materials in geochemistry and environmental research and the

1135 GeoReM database, *Chem. Geol.*, 253, 50–53,  
1136 <https://doi.org/10.1016/j.chemgeo.2008.04.002>, 2008.

1137 Johnson, K.T.M., Dick, H.J.B. and Shimizu, N.: Melting in the oceanic upper mantle: An ion  
1138 microprobe study of diopsides in abyssal peridotites, *J. Geophys. Res.*, 95, 2661–2678,  
1139 <https://doi.org/10.1029/JB095iB03p02661>, 1990.

1140 Juriček, M.P and Keppler, H.: Amphibole stability, water storage in the mantle, and the nature of the  
1141 lithosphere–asthenosphere boundary, *Earth Planet. Sci. Lett.*, 608, 118082,  
1142 <https://doi.org/10.1016/j.epsl.2023.118082>, 2023.

1143 Kaneko, J., Machida, S., Hirano, N., Kasaya, T. and Kumagai, H.: Near bottom MBES survey  
1144 mounted on a HOV at 5500m depth. *Oceans Conference Record (IEEE) 2022*, 1–5,  
1145 <https://doi.org/10.1109/OCEANSChennai45887.2022.9775366>, 2022.

1146 Kang, L. and Karato, S. -I.: Hydrogen Partitioning Between Olivine and Orthopyroxene:  
1147 Implications for the Lithosphere–Asthenosphere Structure, *J. Geophys. Res.*, 128,  
1148 e2022JB025259, <https://doi.org/10.1029/2022JB025259>, 2023.

1149 Karato, S.-I. and Jung, H.: Water, partial melting and the origin of the seismic low velocity and high  
1150 attenuation zone in the upper mantle, *Earth Planet. Sci. Lett.*, 157, 193–207,  
1151 [https://doi.org/10.1016/S0012-821X\(98\)00034-X](https://doi.org/10.1016/S0012-821X(98)00034-X), 1998.

1152 Katsura, T. and Fei, H.: Asthenosphere dynamics based on the H<sub>2</sub>O dependence of element  
1153 diffusivity in olivine, *Natl. Sci. Rev.*, 8, nwaa278. <https://doi.org/10.1093/nsr/nwaa278>,  
1154 2021.

1155 Kawakatsu, H., Kumar, P., Takei, Y., Shinohara, M., Kanazawa, T., Araki, E. and Suyehiro, K.:  
1156 Seismic Evidence for Sharp Lithosphere–Asthenosphere Boundaries of Oceanic Plates,  
1157 *Science*, 324, 499–502, <https://www.science.org/doi/10.1126/science.1169499>, 2009.

1158 Kelemen, P.B., Yogodzinskim G.M., and Scholl, D.W.: Along-strike variation in the Aleutian Island  
1159 Arc: genesis of high Mg# andesite and implications for continental crust, In: Eiler, J. (ed.),  
1160 *Inside the subduction Factory*, American Geophysical Union, Geophysical Monograph, 138,  
1161 223–276, <https://doi.org/10.1029/138GM11>, 2003.

1162 Keshav, S. and Gudfinnsson, G.H.: Silicate liquid–carbonatite liquid transition along the melting curve  
1163 of model, vapor-saturated peridotite in the system CaO–MgO–Al<sub>2</sub>O<sub>3</sub>–SiO<sub>2</sub>–CO<sub>2</sub> from 1.1 to  
1164 2 GPa, *J. Geophys. Res.*, 118, 3341–3353, <https://doi.org/10.1002/jgrb.50249>, 2013.

1165 Kisieva, E.S., Litasov, K.D., Yaxley, G.M., Ohtani, E. and Kamenetsky, V.S.: Melting and Phase  
1166 Relations of Carbonated Eclogite at 9–21 GPa and the Petrogenesis of Alkali-Rich Melts in  
1167 the Deep Mantle, *J. Petrol.*, 54, 1555–1583, <https://doi.org/10.1093/petrology/egt023>, 2013.

1168 Kobayashi, M., Sumino, H., Saito, T., Nagao, K.: Determination of halogens in geological reference  
1169 materials using neutron irradiation noble gas mass spectrometry, *Chem. Geol.*, 582, 120420,  
1170 <https://doi.org/10.1016/j.chemgeo.2021.120420>, 2021.

1171 Konovalov, Y. I. and Martynov, Y. A.: Volcanic complex of the La Mont Guyot; Marcus-Wake Uplift,  
1172 Pacific Ocean, *Pacific Geology*, 5, 40–47, 1992.

1173 Konter, J.G., Hanan, B.B., Blicher-Toft, J., Koppers, A.A.P., Plank, T. and Staudigel, H.: One  
1174 hundred million years of mantle geochemical history suggest the retiring of mantle plumes  
1175 is premature, *Earth Planet Sci Lett*, 275, 285–295,  
1176 <https://doi.org/10.1016/j.epsl.2008.08.023>, 2008.

1177 Koppers, A. A. P., H. Staudigel. and J. R. Wijbrans.: Dating crystalline groundmass separates of  
1178 altered Cretaceous seamount basalts by the Ar<sup>40</sup>/Ar<sup>39</sup> incremental heating technique, *Chem.*  
1179 *Geol.*, 166, 139–158. [https://doi.org/10.1016/S0009-2541\(99\)00188-6](https://doi.org/10.1016/S0009-2541(99)00188-6), 2000.

1180 Koppers, A.A.P., Staudigel, H., Pringle, M.S. and Wijbrans, J.R.: Short-lived and discontinuous  
1181 intra-plate volcanism in the South Pacific: hotspots or extensional volcanism?, *Geochem.*  
1182 *Geophys. Geosyst.*, 4, 1089, <https://doi.org/10.1029/2003GC000533>, 2003.

1183 Korenaga, J.: Plate tectonics and surface environment: Role of the oceanic upper mantle, *Earth Sci.*  
1184 *Rev.*, 205, 103185, <https://doi.org/10.1016/j.earscirev.2020.103185>, 2020.

1185 Le Bas, M. J., Le Maitre, R., Strackeisen, A. and Zanettin, B. (1986) A chemical classification of  
1186 volcanic rocks based on the total alkali–silica diagram, *J. Petrol.*, 27, 745–750,  
1187 <https://doi.org/10.1093/petrology/27.3.745>, 2020.

1188 Lu, C., Grand, S. P., Lai, H. and Garnero, E. J.: TX2019slab: A New P and S Tomography Model  
1189 Incorporating Subducting Slabs, *J. Geophys. Res.*, 124, 11549–11567,  
1190 <https://doi.org/10.1029/2019JB017448>, 2019.

1191 Liu, J., Hirano, N., Machida, S., Xia, Q., Tao, C., Liao, S., Liang, J., Li W., Yang, W. Zhang, G. and  
1192 Ding, T.: Melting of recycled ancient crust responsible for the Gutenberg discontinuity, *Nat.*  
1193 *Commun.*, 11, 172, <https://doi.org/10.1038/s41467-019-13958-w>, 2020.

1194 Longerich, H.P., Jackson, S.E. and Gunther, D.: Laser ablation inductively coupled plasma mass  
1195 spectrometric transient signal data acquisition and analyte concentration calculation, *J. Anal.*  
1196 *At. Spectrom.*, 11, 899–904, <https://doi.org/10.1039/ja9961100899>, 1996.

1197 Machida, S., Hirano, N., and Kimura, J.-I.: Evidence for recycled material in Pacific upper mantle  
1198 unrelated to plumes, *Geochim. Cosmochim. Acta.*, 73, 3028–3037,  
1199 <http://dx.doi.org/10.1016/j.gca.2009.01.026>, 2009.

1200 Machida, S., Orihashi, Y., Magnani, M., Neo, N., Wilson, S., Tanimizu, M., Yoneda, S., Yasuda, A.  
1201 and Tamaki, K.: Regional mantle heterogeneity regulates melt production along the Réunion  
1202 hotspot-influenced Central Indian Ridge, *Geochem. J.*, 48, 433–449,  
1203 <https://doi.org/10.2343/geochemj.2.0320>, 2014.

1204 Machida, S., Hirano, N., Sumino, H., Hirata, T., Yoneda, S. and Kato, Y: Petit-spot geology reveals  
1205 melts in upper-most asthenosphere dragged by lithosphere, *Earth Planet. Sci. Lett.*, 426,  
1206 267–279, <https://doi.org/10.1016/j.epsl.2015.06.018>, 2015

1207 Machida, S., Fujinaga, K., Ishii, T., Nakamura, K., Hirano, N. and Kato, Y.: Geology and  
1208 geochemistry of ferromanganese nodules in the Japanese Exclusive Economic Zone around  
1209 Minamitorishima Island, *Geochem. J.*, 50, 539–555,  
1210 <https://doi.org/10.2343/geochemj.2.0419>, 2016.

1211 Machida, S., Kogiso, T. and Hirano, N.: Petit-spot as definitive evidence for partial melting in the  
1212 asthenosphere caused by CO<sub>2</sub>, *Nat. Commun.*, 8, 14302,  
1213 <https://doi.org/10.1038/ncomms14302>, 2017.

1214 Massuyeau, M., Gardés, E., Morizet, Y. and Gaillard, F.: A model for the activity of silica along the  
1215 carbonatite–kimberlite–mellilitite–basanite melt compositional joint, *Chem. Geol.*, 418,  
1216 206–216, <https://doi.org/10.1016/j.chemgeo.2015.07.025>, 2015.

1217 Massuyeau, M., Gardés, E., Rogerie, G., Aulbach, S., Tappe, S., Le Trong, E., Sifré, D. and Gaillaer,  
1218 F.: MAGLAB: A computing platform connecting geophysical signatures to melting  
1219 processes in Earth's mantle, *Phys. Earth Planet.*, 314, 106638,  
1220 <https://doi.org/10.1016/j.pepi.2020.106638>, 2021.

1221 McKenzie, D. and O'Nions, R.K.: Partial melt distributions from inversion of rare Earth element  
1222 concentrations, *J. Petrol.*, 32, 1021–1091, <https://doi.org/10.1093/petrology/32.5.1021>,  
1223 1991.

1224 McKenzie, D. and O'Nions, R.K.: The Source Regions of Ocean Island Basalts, *J. Petrol.*, 36, 133–  
1225 159, <https://doi.org/10.1093/petrology/36.1.133>, 1995.

1226 Melson, W.G., Thompson, G. and van Andel, T.H.: Volcanism and metamorphism in the Mid-  
1227 Atlantic Ridge, 22°N latitude, *J. Geophys. Res.*, 73, 5925–5941,  
1228 <https://doi.org/10.1029/JB073i018p05925>, 1968.

1229 Mierdel, K., Keppler, H., Smyth, J.R. and Langenhorst, F.: Water solubility in aluminous  
1230 orthopyroxene and the origin of Earth's Asthenosphere, *Science*, 315, 364–368,  
1231 <https://doi.org/10.1126/science.1135422>, 2007.

1232 Mikuni, K., Hirano, N., Akizawa, N., Yamamoto, J., Machida, S., Tamura, A., Hagiwara, Y.,  
1233 Morishita, T.: Lithological structure of western Pacific lithosphere reconstructed from  
1234 mantle xenoliths in a petit-spot volcano, *Prog. Earth Planet. Sci.*, 9, 62,  
1235 <https://doi.org/10.1186/s40645-022-00518-y>, 2022.

1236 Miyashiro, A., Shido, F. and Ewing, M.: Metamorphism on the Mid-Atlantic Ridge near 24 and 30°  
1237 N. *Phil. Trans. Roy. Soc. Lond.*, 268, 589–603, <https://doi.org/10.1098/rsta.1971.0014>,  
1238 1971.

1239 Morimoto, N.: Nomenclature of pyroxenes. *Mineral. Petrol.*, 39, 55–76,  
1240 <https://doi.org/10.1007/BF01226262>, 1988.

1241 Moore, J.G., Fornari, D.J. and Clague, D.A.: Basalts from the 1877 Submarine Eruption of Mauna  
1242 Loa, Hawaii; New Data on the Variation of Palagonitization Rate with Temperature. United

1243 States Geol. Surv. Bull. 1663., 1–11, <https://doi.org/10.3133/b1663>, 1985.

1244 Müller, R.D., Sdrolias, M., Gaina, C. and Roest, W.R.: Age, spreading rates, and spreading  
1245 asymmetry of the world's ocean crust. *Geochem. Geophys. Geosyst.*, 9, Q04006.  
1246 <http://dx.doi.org/10.1029/2007GC001743>, 2008.

1247 Natland, J.: Petrology of Volcanic Rocks Dredged from Seamounts in the Line Islands, *Init. Rep.*  
1248 *Deep Sea Drill. Proj.*, 33, 749–777. <https://doi.org/10.2973/dsdp.proc.33.126.1976>, 1976.

1249 Nier, A.: A redetermination of the relative abundances of the isotopes of carbon, nitrogen, oxygen,  
1250 argon, and potassium, *Phys. Rev.*, 77, 789–793, <https://doi.org/10.1103/PhysRev.77.789>,  
1251 1950.

1252 Nobre Silva, I.G., Weis, D., Barling, J. and Scoates, J.S.: Leaching systematics and matrix  
1253 elimination for the determination of high-precision Pb isotope compositions of ocean island  
1254 basalts, *Geochem. Geophys. Geosyst.*, 10, Q08012, <https://doi.org/10.1029/2009GC002537>,  
1255 2009.

1256 Novella, D., Keshav, S., Gudfinnsson, G.H. and Ghosh, S.: Melting phase relations of model  
1257 carbonated peridotite from 2 to 3 GPa in the system CaO-MgO-Al<sub>2</sub>O<sub>3</sub>-SiO<sub>2</sub>-CO<sub>2</sub> and further  
1258 indication of possible unmixing between carbonatite and silicate liquids, *J. Geophys. Res.*,  
1259 119, 2780–2800, <https://doi.org/10.1002/2013JB010913>, 2014.

1260 Nozaki, T., Tokumaru, A., Takaya, Y., Kato, Y., Suzuki, K. and Urabe, T.: Major and trace element  
1261 compositions and resource potential of ferromanganese crust at Takuyo Daigo Seamount,  
1262 northwestern Pacific Ocean, *Geochem J.*, 50, 527–537,  
1263 <https://doi.org/10.2343/geochemj.2.0430>, 2016.

1264 Okumura, S. and Hirano, N.: Carbon dioxide emission to earth's surface by deep-sea volcanism,  
1265 *Geology*, 41, 1167–1170, <https://doi.org/10.1130/G34620.1>, 2013.

1266 Orihashi, Y., Maeda, J., Tanaka, R., Zeniya, R. and Niida, K.: Sr and Nd isotopic data for the seven  
1267 GSJ rock reference samples; JA-1, JB-1a, JB-2, JB-3, JG-1a, JGb-1 and JR-1, *Geochem. J.*,  
1268 32, 205–211, <https://doi.org/10.2343/geochemj.32.205>, 1998.

1269 Ozawa, K.: Mass balance equations for open magmatic systems: Trace element behavior and its  
1270 application to open system melting in the upper mantle. *J. Geophys. Res.*, 106, 13407–  
1271 13434, <https://doi.org/10.1029/2001JB900001>, 2001.

1272 Pearce, N.J.G., Perkins, W.T., Westgate, J.A., Gorton, M.P., Jackson, S.E., Neal, C.R. and Chenery,  
1273 S.P.: A compilation of new and published major and trace element data for NIST SRM 610  
1274 and NIST SRM 612 glass reference materials, *Geostand. Newsl.*, 21, 115–144,  
1275 <https://doi.org/10.1111/j.1751-908X.1997.tb00538.x>, 1997.

1276 Pilet, S., Baker, M.B. and Stolper, E.M.: Metasomatized Lithosphere and the Origin of Alkaline  
1277 Lavas, *Science*, 320, 916–919, <https://doi.org/10.1126/science.1156>, 2008.

1278 Pilet, S.: Generation of low-silica alkaline lavas: Petrological constraints, models, and thermal

1279                   implications, The Interdisciplinary Earth: A Volume in Honor of Don L. Anderson, Gillian  
1280                   R. Foulger, Michele Lustrino, Scott D. King. [https://doi.org/10.1130/2015.2514\(17\)](https://doi.org/10.1130/2015.2514(17)), 2015.

1281                   Pilet, S., Abe, N., Rochat, L., Kaczmarek, M.-A., Hirano, N., Machida, S., Buchs, D.M.,  
1282                   Baumgarther, P.O. and Müntener, O.: Pre-subduction metasomatic enrichment of the oceanic  
1283                   lithosphere induced by plate flexure, *Nat. Geosci.*, 9, 898–903,  
1284                   <https://doi.org/10.1038/ngeo2825>, 2016.

1285                   Regelous, M., Weinzierl, C.G. and Haase, K.M.: Controls on melting at spreading ridges from  
1286                   correlated abyssal peridotite – mid-ocean ridge basalt compositions, *Earth Planet. Sci. Lett.*,  
1287                   449, 1–11. <http://dx.doi.org/10.1016/j.epsl.2016.05.017>, 2016.

1288                   Reinhard, A.A., Jackson, M.G., Blusztajn, J., Koppers, A.A.P., Simms, A.R. and Konter, J.G.: “Petit  
1289                   Spot” Rejuvenated Volcanism Superimposed on Plume-Derived Samoan Shield Volcanoes:  
1290                   Evidence From a 645-m Drill Core From Tutuila Island, American Samoa, *Geochem.  
1291                   Geophys. Geosys.*, 20, 1485–1507, <https://doi.org/10.1029/2018GC007985>, 2019.

1292                   Resing, J.A. and Sansone, F.J.: The chemistry of lava–seawater interactions: the generation of  
1293                   acidity, *Geochim. Cosmochim. Acta.*, 63, 2183–2198, [https://doi.org/10.1016/S0016-7037\(99\)00193-3](https://doi.org/10.1016/S0016-<br/>1294                   7037(99)00193-3), 1999.

1295                   Rohrbach, A., Ballhaus, C., Golla-Schindler, U., Ulmer, P., Kamenetsky, V.S. and Kuzmin, D.V.:  
1296                   Metal saturation in the upper mantle, *Nature*, 449, 456–458,  
1297                   <https://doi.org/10.1038/nature06183>, 2007.

1298                   Rychert, C. A. and Shearer, P. M.: A global view of the lithosphere–asthenosphere boundary,  
1299                   *Science*, 324, 495–498, <https://www.science.org/doi/10.1126/science.1169754>, 2009.

1300                   Sakamaki, T., Suzuki, A., Ohtani, E., Terasaki, H., urakawa, S., Katayama, Y., Funakoshi, K.-I.,  
1301                   Wang, Y. Hernlund, J.H. and Ballmer, M.D.: Ponded melt at the boundary between the  
1302                   lithosphere and asthenosphere, *Nat. Geosci.*, 6, 1041–1044,  
1303                   <https://doi.org/10.1038/ngeo1982>, 2013.

1304                   Shaw, D.M.: Trace element fractionation during anataxis, *Geochim. Cosmochim. Acta.*, 34, 237–  
1305                   243, [https://doi.org/10.1016/0016-7037\(70\)90009-8](https://doi.org/10.1016/0016-7037(70)90009-8), 1970.

1306                   Shaw, C.S.J.: Dissolution of orthopyroxene in basanitic magma between 0.4 and 2 GPa: Further  
1307                   implications for the origin of Si-rich alkaline glass inclusions in mantle xenoliths, *Contrib.  
1308                   Mineral. Petrol.*, 135, 114–132, <https://doi.org/10.1007/s004100050501>, 1999.

1309                   Sifré, D., Gardés, E., Massuyseau, M., Hashim, L., Hier-Majumder, S. and Gaillard, F.: Electrical  
1310                   conductivity during incipient melting in the oceanic low-velocity zone, *Nature*, 509, 81–85,  
1311                   <https://doi.org/10.1038/nature13245>, 2014.

1312                   Smith, W.H.F., Staudigel, H., Watts, A.B. and Pringle, M.S.: The Magellan seamounts: early  
1313                   Cretaceous record of the South Pacific isotopic and thermal anomaly, *J. Geophys. Res.*, 94,  
1314                   10501–10523, <https://doi.org/10.1029/JB094iB08p10501>, 1989.

1315 Staudigel, H. and Hart, S.R.: Alteration of basaltic glass: processes and significance for the oceanic  
1316 crust-seawater budget, *Geochim. Cosmochim. Acta.*, 47, 337–350,  
1317 [https://doi.org/10.1016/0016-7037\(83\)90257-0](https://doi.org/10.1016/0016-7037(83)90257-0), 1983.

1318 Staudigel, H., Park, K.H., Pringle, M., Rubenstone, J.L., Smith, W.H.F. and Zindler, A.: The  
1319 longevity of the South-Pacific isotopic and thermal anomaly, *Earth Planet. Sci. Lett.*, 102,  
1320 24–44, [https://doi.org/10.1016/0012-821X\(91\)90015-A](https://doi.org/10.1016/0012-821X(91)90015-A), 1991.

1321 Stixrude, L. and Lithgow-Bertelloni, C.: Thermodynamics of mantle minerals — I. Physical  
1322 properties, *Geophys. J. Int.*, 162, 610–632, <https://doi.org/10.1111/j.1365-246X.2005.02642.x>, 2005.

1324 Stoermer, R.W., Schaeffer, O.A. and Katcoff, S.: Half-lives of argon-37, argon-39, and argon-42,  
1325 *Science*, 148, 1325–1328, <https://doi.org/10.1126/science.148.3675.1325>, 1965.

1326 Stracke A., Michael, W., Felix, G., Paul, B. and Erin, T.: Major and trace element concentrations and  
1327 Sr, Nd, Hf, Pb isotope ratios of global mid ocean ridge and ocean island basalts, GRO data,  
1328 V1, <https://doi.org/10.25625/0SVW6S>, 2022.

1329 Sun, S.-S. and McDonough, W.F.: Chemical and isotopic systematics of oceanic basalts: implications  
1330 for mantle composition and processes, *Geol. Soc. Spec. Publ.*, 42, 313–345,  
1331 <https://doi.org/10.1144/GSL.SP.1989.042.01.19>, 1989.

1332 Takahashi, E.: Origin of basaltic magmas: Implications from peridotite melting experiments and an  
1333 olivine fractionation model (in Japanese with English abstract), *Bull. Volcanol. Soc. Jpn.*,  
1334 2nd Ser, 30, S17–S40, [https://doi.org/10.18940/kazanc.30.TOKUBE\\_S17](https://doi.org/10.18940/kazanc.30.TOKUBE_S17), 1986.

1335 Takahashi, E., Uto, K. and Schilling, J.-G.: Primary magma compositions and Mg/Fe ratios of their  
1336 mantle residues along Mid Atlantic Ridge 29° N to 73°N, Technical Report of ISEI  
1337 Okayama University Series A, 9, 1–4, 1987.

1338 Tamura, A., Arai, S., Takeuchi, M., Miura, M. and Pirnia, T.: Compositional heterogeneity of a  
1339 websterite xenolith from Kurose, southwest Japan: insights into the evolution of lower crust  
1340 beneath the Japan Arc, *Eur. J. Mineral.*, 31, 35–47, <https://doi.org/10.1127/ejm/2018/0030-2803>, 2019.

1342 Taneja, R., Rushmer, T., Blichert-Toft, J., Turner, S. and O'Neill, C.: Mantle heterogeneities beneath  
1343 the Northeast Indian Ocean as sampled by intra-plate volcanism at Christmas Island, *Lithos*,  
1344 262, 561–575, <http://dx.doi.org/10.1016/j.lithos.2016.07.027>, 2016.

1345 Tanimizu, M. and Ishikawa, T.: Development of rapid and precise Pb isotope analytical techniques  
1346 using MC-ICPMS and new results for GSJ rock reference samples, *Geochem. J.*, 40, 121–  
1347 133. <https://doi.org/10.2343/geochemj.40.121>, 2006.

1348 Tatsumi, Y., Sakuyama, M., Fukuyama, H. and Kushiro, I.: Generation of arc basalt magmas and  
1349 thermal structure of the mantle wedge in subduction zones, *J. Geophys. Res.*, 88, 5815–  
1350 5825, <https://doi.org/10.1029/JB088iB07p05815>, 1983.

1351 Tivey, M.A., Sager, W.W., Lee, S.-M. and Tominaga, M.: Origin of the Pacific Jurassic quiet zone,  
1352 Geology, 34, 789–792, <https://doi.org/10.1130/G22894.1>, 2006.

1353 Uenzelmann-Neben, G., Schmidt, D.N., Niessen, F. and Stein, R.: Intraplate volcanism off South  
1354 Greenland: caused by glacial rebound?, Geophys. J. Int., 190, 1–7,  
1355 <https://doi.org/10.1111/j.1365-246X.2012.05468.x>, 2012.

1356 Valentine, G.A. and Hirano, N.: Mechanisms of low-flux intraplate volcanic fields—Basin and  
1357 Range (North America) and northwest Pacific Ocean, Geology, 38, 55–58,  
1358 <https://doi.org/10.1130/G30427.1>, 2010.

1359 Walter, M.J.: Melting of garnet peridotite and the origin of komatiite and depleted lithosphere, J.  
1360 Petrol., 39, 29–60, <https://doi.org/10.1093/petroj/39.1.29>, 1998.

1361 Wakaki, S., Shibata, S.-N. and Tanaka, T.: Isotope ratio measurements of trace Nd by the total  
1362 evaporation normalization (TEN) method in thermal ionization mass spectrometry, Int. J.  
1363 Mass Spectrom., 264, 157–163, <http://dx.doi.org/10.1016/j.ijms.2007.04.006>, 2007.

1364 Wang, D., Mookherjee, M., Xu, Y. and Karato, S.-I.: The effect of water on the electrical conductivity  
1365 of olivine, Nature, 443, 977–980, <https://doi.org/10.1038/nature05256>, 2006.

1366 Wang, X.-J., Chen, L.-H., Hofmann, A.W., Hanyu, T., Kawabata, H., Zhong, Y., Xie, L.-W., Shi, J.-  
1367 H., Miyazaki, T., Hirata, Y., Takahashi, T., Senda, R., Chang, O., Vaglarov, B.S. and Kimura,  
1368 J.-I. Recycled ancient ghost carbonate in the Pitcairn mantle plume, PNAS, 115, 8682–8687,  
1369 <https://doi.org/10.1073/pnas.1719570115>, 2018.

1370 Weis, D. and Frey, F.A.: Isotope geochemistry of the Ninetyeast Ridge basement basalts: Sr, Nd, and  
1371 Pb evidence for involvement of the Kerguelen hot spot, Proc. Ocean Drill. Program Sci.  
1372 Results, 121, 591–610, 1991.

1373 Weis, D. and Frey, F.A.: Role of the Kerguelen Plume in generating the eastern Indian Ocean  
1374 seafloor. J. Geophys. Res., 101, 13381–13849, <https://doi.org/10.1029/96JB00410>, 1996.

1375 Weis, D., Kieffer, B., Maerschalk, C., Barling, J., de Jong, J., Williams, G.A., Hanano, D., Pretorius,  
1376 W., Mattielli, N., Scoates, J.S., Goolaerts, A., Friedman, R. M. and Mahoney, J.B.: High-  
1377 precision isotopic characterization of USGS reference materials by TIMS and MC-ICP-MS,  
1378 Geochem. Geophys. Geosyst., 7, Q08006, <http://dx.doi.org/10.1029/2006GC001283>, 2006.

1379 Weiss, Y., Class, C., Goldstein, S.L. and Hanyu, T.: Key new pieces of the HIMU puzzle from  
1380 olivines and diamond inclusions, Nature, 537, 666–670,  
1381 <https://doi.org/10.1038/nature19113>, 2016.

1382 [Wessel, P., Luis, J.F., Uieda, L., Scharroo, R., Wobbe, F., Smith, W.H.F., and Tian, D.: The Generic](#)  
1383 [Mapping Tools version 6, Geochem Geophys Geosyst., 20, 5556–5564,](#)  
1384 [https://doi.org/10.1029/2019GC008515. 2019.](#)

1385 Workman, R.K., Hart, S.R., Jackson, M., Regelous, M., Farley, K.A., Blusztajn, J., Kurz, M. and  
1386 Staudigel, H.: Recycled metasomatized lithosphere as the origin of the Enriched Mantle II

1387 (EM2) end-member: Evidence from the Samoan Volcanic Chain, *Geochem. Geophys.*  
1388 *Geosyst.*, 5, Q04008, <https://doi.org/10.1029/2003GC000623>, 2004.

1389 Yamamoto, J., Hirano, N., Abe, N. and Hanyu, T.: Noble gas isotopic compositions of mantle  
1390 xenoliths from northwestern Pacific lithosphere, *Chem. Geol.*, 268, 313–323,  
1391 <https://doi.org/10.1016/j.chemgeo.2009.09.009>, 2009.

1392 Yamamoto, J., Korenaga, J., Hirano, N. and Kagi, H.: Melt-rich lithosphere-asthenosphere boundary  
1393 inferred from petit-spot volcanoes, *Geology*, 42, 967–970,  
1394 <https://doi.org/10.1130/G35944.1>, 2014.

1395 Yamamoto, J., Kawano, T., Takahata, N. and Sano, Y.: Noble gas and carbon isotopic compositions  
1396 of petit-spot lavas from southeast of Marcus Island. *Earth Planet. Sci. Lett.*, 497, 139–148,  
1397 <https://doi.org/10.1016/j.epsl.2018.06.020>, 2018.

1398 Yamamoto, J., Hirano, N. and Kurz, M.D.: Noble gas isotopic compositions of seamount lavas from  
1399 the central Chile trench: Implications for petit-spot volcanism and the lithosphere  
1400 asthenosphere boundary, *Earth Planet. Sci. Lett.*, 552, 116611,  
1401 <https://doi.org/10.1016/j.epsl.2020.116611>, 2020.

1402 Yamazaki, S., Neo, N. and Miyashita, S.: Data report: whole-rock major and trace elements and  
1403 mineral compositions of the sheeted dike–gabbro transition in ODP Hole 1256D, In Teagle,  
1404 D. A. H., Alt, J. C., Umino, S., Miyashita, S., Banerjee, N. R., Wilson, D. S. and the  
1405 Expedition 309/312 Scientists (Eds.), *Proceedings Integrated Ocean Drilling Program.*  
1406 309/312: Washington, DC (Integrated Ocean Drilling Program Management International,  
1407 Inc.) <https://doi.org/10.2204/iodp.proc.309312.203.2009>, 2009.

1408 Yang, H.-J., Frey, F.A. and Clague, D.A.: Constraints on the Source Components of Lavas Forming  
1409 the Hawaiian North Arch and Honolulu Volcanics, *J. Petrol.*, 44, 603–627,  
1410 <https://doi.org/10.1093/petrology/44.4.603>, 2003.

1411 Yoshino, T., Matsuzaki, T., Yamashita, S. and Katsura T.: Hydrous olivine unable to account for  
1412 conductivity anomaly at the top of the asthenosphere, *Nature*, 443, 973–976,  
1413 <https://doi.org/10.1038/nature05223>, 2006.

1414 Zakharov, D.O., Tanaka, R., Butterfield, D.A. and Nakamura, E.: A New Insight Into Seawater-  
1415 Basalt Exchange Reactions Based on Combined  $\delta^{18}\text{O}$ — $\Delta^{17}\text{O}$ — $^{87}\text{Sr}/^{86}\text{Sr}$  Values of  
1416 Hydrothermal Fluids From the Axial Seamount Volcano, Pacific Ocean. *Front. Earth Sci.*, 9,  
1417 691699, <https://doi.org/10.3389/feart.2021.691699>, 2021.

1418 Zhang, F., Lin, J. and Zhan, W.: Variations in oceanic plate bending along the Mariana trench. *Earth*  
1419 *Planet. Sci. Lett.*, 401, 206–214, <http://dx.doi.org/10.1016/j.epsl.2014.05.032>, 2014.

1420 Zhang, G.L., Chen, L.H., Jackson, M. and Hofmann, A.W.: Evolution of carbonated melt to alkali  
1421 basalt in the South China Sea, *Nat. Geosci.*, 10, 229–235, <https://doi.org/10.1038/ngeo2877>,  
1422 2017.

1423 Zhang, W., Johnston, S. and Currie, C.A., Kimberlite magmatism induced by west-dipping  
1424 subduction of the North American plate, *Geology*, 47, 395–398,  
1425 <https://doi.org/10.1130/G45813.1>, 2019.

1426 Zhang, J., Xu, M. and Sun, Z.: Lithospheric flexural modelling of the seaward and trenchward of the  
1427 subducting oceanic plates, *Int. Geol. Rev.*, 62, 908–923,  
1428 <https://doi.org/10.1080/00206814.2018.1550729>, 2020.

1429 Zhang, G., Wang, S., Huang, S., Zhan, M. and Yao, J.: CO<sub>2</sub>-rich rejuvenated stage lavas on Hawaiian  
1430 Islands, *Geochem. Geophys. Geosyst.*, 23, e2022GC010525,  
1431 <https://doi.org/10.1029/2022GC010525>, 2022.

1432 Zhong, Y., Zhang, G.-L., Zhong, L.-F., Chen, L.-H. and Wang, X.-J.: Post-spreading volcanism  
1433 triggered by CO<sub>2</sub> along the South China Sea fossil spreading axis, *Lithos*, 404–405, 106478,  
1434 <https://doi.org/10.1016/j.lithos.2021.106478>, 2021.

1435 Zindler, A. and Hart, S.: Chemical geodynamics, *Ann. Rev. Earth Planet. Sci.*, 14, 493–571,  
1436 <https://doi.org/10.1146/annurev.ea.14.050186.002425>, 1986.